Influence of Quenching Temperature and Mn Content on the Microstructure Development of New Q&P Processed Martensitic Stainless Steels

by

Benne de Bakker

to obtain the degree of Master of Science
at the Delft University of Technology,
to be defended publicly on Friday March 19, 2021 at 13:00

Student number:	4356810	
Thesis committee:	Prof.dr. M.J. Santofimia Navarro	TU Delft, promotor and supervisor
	G. Li	TU Delft, supervisor
	Dr. Y. Gonzalez Garcia	TU Delft
	Ing. C. Kwakernaak	TU Delft
	Dr. A. Smith	RINA S.p.A.

TU Delft

QPINOX
Development of New Martensitic Stainless Steels for Automotive Lightweight Structural Applications

Acknowledgements

I would like to express my sincere gratitude to Professor Maria J. Santofimia Navarro for her guidance and supervision of this research project. I appreciate your valuable feedback and support during the writing of this thesis and the challenging period surrounding the COVID-19 pandemic. I would also like to acknowledge the partners of the QPINOX project; Acerinox Europa, IMDEA Materials, RINA-CSM and TU Delft, who supplied the materials for this study and provided funding through the European Union's Research Fund for Coal and Steel.

I wish to thank my daily supervisor, Gaojie Li, for her support and assistance with the experiments. I appreciate that you were always available for questions and willing to help where needed.

I would also like to acknowledge the technicians of the Department of Materials Science and Engineering of Delft University of Technology. Many thanks to Sander van Asperen and Luís de Almeida Nieto for providing training and practical tips on sample preparation. I thank Nico Geerlofs and Gaojie Li for performing the dilatometry experiments and the X-ray facilities group for their assistance in performing XRD measurements. I would also like to extend my deepest gratitude to Kees Kwakernaak for his help with microstructure analysis using EBSD and EPMA and to Pina Mecozzi for performing phase field simulations of the studied alloys.

Finally, I would like to thank my family and fellow master students for their encouragement and pleasant conversations during this project.

Benne de Bakker
Delft, February 2021

Abstract

Quenching and Partitioning (Q&P) is a novel steel heat treatment to create microstructures containing martensite and retained austenite. In recent years, there has been a growing interest in applying Q&P treatments to martensitic stainless steels with the aim to create stainless steels with the mechanical properties of Advanced High-Strength Steels (AHSS). The development of Q&P stainless steels for lightweight structural applications could be a game changer for the automotive industry. The application of Q&P stainless steels can increase the service life of a car, reduce maintenance cost and contribute to lowering CO_2 emissions.

In this thesis, Q&P treatments with varying quenching temperatures were applied to two novel stainless steel alloys with composition 0.2C-0.35Si-0.7Mn-12.5Cr and 0.2C-0.35Si-3.0Mn-12.5Cr. The effect of quenching temperature and Mn content on the microstructure development was investigated using dilatometry, X-ray diffraction (XRD), optical microscopy, electron backscatter diffraction (EBSD), electron probe micro analysis (EPMA) and phase field simulations. It was found that Mn addition lowers the optimal quenching temperature and increases the maximum retained austenite fraction that can be obtained by Q&P treatment. Austenite phase fractions of approximately 0.22 and 0.3 were stabilized in the microstructures of the low-Mn and the high-Mn alloy, respectively. The carbon concentration of retained austenite increases with decreasing quenching temperature but is much lower than expected from the full partitioning assumption. The non-uniform distribution of primary martensite and untransformed austenite as well as carbide precipitation was seen as a means by which austenite enrichment and retention are reduced. Additionally, results from this study indicate that segregation of Mn and Cr affects the local M_S temperature and causes microstructural banding of primary martensite which leads to a non-uniform retained austenite distribution in the final microstructure.

Contents

List of Figures

List of Tables

Chapter 1

Introduction

In recent years, legislation on CO_2 emission reduction and passenger safety of automobiles has pressured the automotive industry to produce lighter and safer cars. These increased demands require higher strength materials with good combinations of strength, formability, cost and toughness. For this reason, the steel industry has been developing a new "third generation" of advanced high-strength steels (AHSS). These new steels, in particular quenching and partitioning (Q&P) steels, are characterized by a significant improvement in the strength-ductility balance compared to first generation AHSS, such as dual-phase (DP), martensitic (MS) and transformation-induced plasticity (TRIP) steels. In addition, they cost significantly less than second generation AHSS, such as twinning-induced plasticity (TWIP) steels which require high levels of alloying elements. Q&P steels thereby fill the property gap between first and second generation AHSS and provide the needed balance between cost, strength and formability (Figure 1.1).[1]

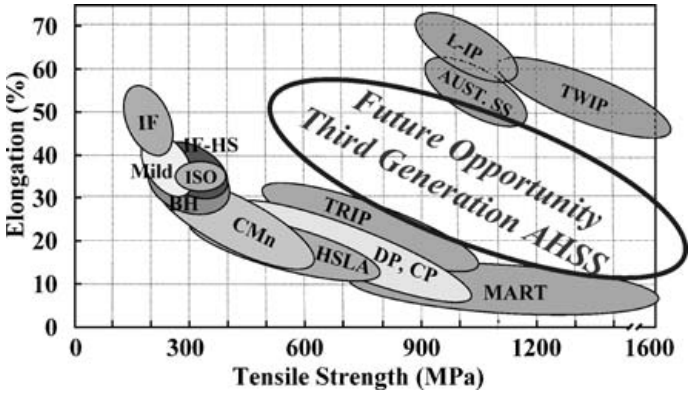

Figure 1.1: Summary of tensile strength and elongation data for different classes of conventional and advanced high-strength steel grades. Q&P steels are considered part of the third generation of AHSS.[1]

The enhanced mechanical properties of Q&P steels are achieved by stabilizing austenite to room temperature and combining the strength of martensite with the transformation-induced plasticity (TRIP) effect of retained austenite during deformation. The multi-step quenching and partitioning process is a method of stabilizing austenite to room temperature by partial martensitic transformation and carbon partitioning from carbon-supersaturated martensite into untransformed austenite.

Since the first proposal of the Q&P concept by Speer et al.[2] in 2003, many researchers have investigated the relationships between processing, microstructures and properties of Q&P steels.[3] Considerable progress in the understanding and industrialization of the quenching and partitioning process has already been made, but most research has focused on steels that are not corrosion-resistant. More recently, there has been a growing interest in applying the Q&P treatment to other steel grades as well, in particular martensitic stainless steels.[4]

The development of Q&P stainless steels could be a game changer for the automotive industry as it can increase the service life of a car, reduce maintenance and contribute to achieving the CO_2 emission reduction targets. However, the toughness and ductility of currently available martensitic stainless steels such as AISI 410 (Fe-12Cr-0.1C) and AISI 420 (Fe-12Cr-0.3C) are insufficient for structural applications.[5, 6] Therefore, to increase the applicability of these stainless steels, their strength-ductility balance needs to be improved to meet the industry demands and match the mechanical properties of AHSS. Several researchers have shown that similarly to other steel grades, the dispersion of retained austenite can greatly improve the toughness and formability of common martensitic stainless steels.[4, 7, 8] In low-alloyed steels with a martensite-finish temperature higher than room temperature, there are three methods to retain a sufficient amount of austenite at room temperature. The first method consists of a partial reversion treatment of martensite, but requires alloying with high amounts of nickel or manganese. The second method involves austempering to form bainite, where the austenite is enriched with carbon and its martensite-start temperature is lowered to below room temperature.[9, 10] However, this method is impossible to apply to stainless steels, because the transformation of austenite to bainite is inhibited by the high chromium contents. Therefore, the third method, Q&P processing, is the only method to obtain retained austenite in low-carbon martensitic stainless steels.[7]

Careful selection of Q&P processing parameters and steel chemistry optimization is crucial for obtaining the desired combination of mechanical properties, corrosion resistance and production costs. In particular, the choice of quenching temperature (QT) is of primary importance in obtaining the highest retained austenite fraction. Although models have been developed to predict the influence of Q&P processing parameters on microstructure development, experimental research is still needed to determine an optimal Q&P treatment for a given steel alloy. This is especially the case for martensitic stainless steels, which to date have been studied in less detail compared to other Q&P steels.

1.1 Objective and structure of the thesis

The main goal of this thesis is to experimentally investigate the influence of quenching temperature and manganese content on the microstructure development during Q&P processing of martensitic stainless steels. Q&P treatments were performed for two novel stainless steel alloys containing 0.2 wt.% carbon and different amounts of manganese (0.7 and 3.0 wt.%). These alloys were designed as part of the QPINOX project [11], which aims to generate a new class of affordable martensitic stainless steels for the automotive sector. This research project, entitled 'Development of New Martensitic Stainless Steels for Automotive Lightweight Structural Applications (QPINOX)', is led by a consortium of industry and research partners and has received funding from the Research Fund for Coal and Steel (RFCS) of the European Union. The consortium consists of the stainless steel manufacturer Acerinox Europa, the research institutes IMDEA Materials and RINA-CSM

and Delft University of Technology. The two objectives of the project are to develop new martensitic stainless steel grades containing retained austenite by using Q&P processing and chemistry optimization and to facilitate the industrial implementation of these new grades.

More specifically for this thesis, the main research questions are as follows:

- How does quenching temperature affect the volume fraction and carbon enrichment of retained austenite in two different Q&P processed martensitic stainless steels?
- What is the correlation between Mn content and microstructure development during Q&P processing of martensitic stainless steels?

In this thesis, Q&P treatments were performed using a dilatometer, followed by microstructure characterization using optical microscopy (OM), X-ray diffraction (XRD), electron backscatter diffraction (EBSD), and electron probe micro analysis (EPMA). Additionally, a phase field simulation was performed to simulate the carbon enrichment of austenite during the partitioning step.

In chapter 2 of this thesis, a brief overview and relevant background information of the Q&P treatment is given. The studied materials and the experimental methods used to obtain the results reported herein can be found in chapter 3. In chapter 4 and 5, the obtained experimental results are presented and discussed. Finally, in chapter 6, the concluding remarks are presented along with recommendations for future research.

Chapter 2

Background

2.1 Overview of the quenching and partitioning treatment

An overview of a typical Q&P process is given in Figure 2.1. The process starts with partial or full austenitization of the steel above the Ac_3 temperature. After austenitization, the steel is transformed into a controlled fraction of martensite by quenching to a temperature QT between the martensite-start temperature (M_S) and the martensite-finish temperature (M_F). The latter is frequently defined as the point where 95 % of the martensitic transformation is completed. Alloys with an M_F temperature below room temperature (RT) can therefore be compatible with a simpler Q&P treatment with QT equal to RT. After quenching, the multiphase material consisting of untransformed austenite and primary martensite (M_1) is heated to a higher temperature PT where carbon can partition from the carbon-supersaturated martensite into the untransformed austenite. The carbon enrichment of the untransformed austenite lowers its M_S temperature and leads to stabilization of the austenite upon cooling to room temperature. If part of the austenite is not sufficiently enriched with carbon, it transforms into fresh martensite (M_2) during the final quench to room temperature. Therefore, an optimal quenching temperature OQT can be defined as the QT for which the maximum amount of austenite is retained and the M_S temperature of the carbon enriched austenite is equal to RT, i.e. no M_2 forms. The final microstructure after Q&P processing therefore typically consists of:

- M_1 - primary martensite formed during the initial quench to QT that is tempered during the partitioning step.
- RA - retained austenite stabilized to room temperature at the end of the heat treatment.
- M_2 - fresh/secondary martensite that forms during the final quench to room temperature (only forms when the untransformed austenite is not sufficiently enriched with carbon).

The volume fraction and mechanical stability of retained austenite strongly influence the mechanical properties of steels and are important factors to consider when designing a suitable Q&P process.[8]

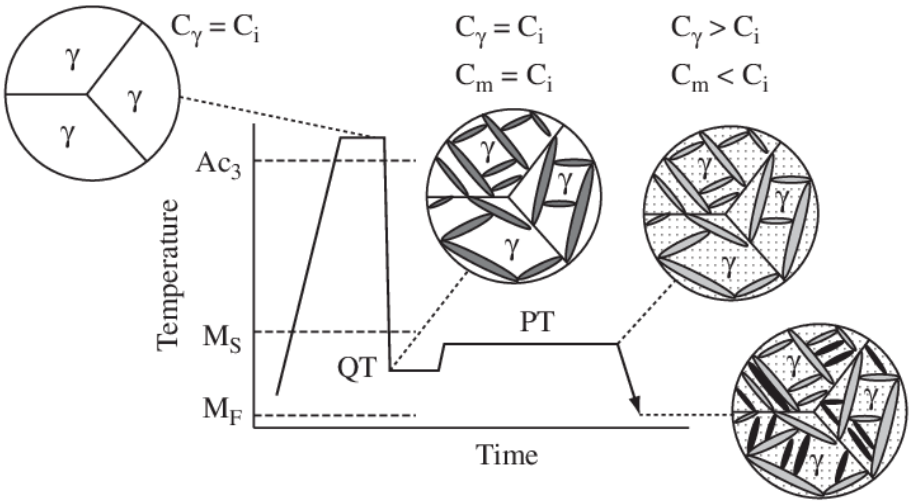

Figure 2.1: Schematic heat-treatment diagram of the quenching and partitioning (Q&P) process. C_i, C_γ and C_m represent the carbon concentrations in the initial alloy, austenite, and martensite, respectively.[12]

In 2003, Speer et al.[2] developed a thermodynamic model that describes the endpoint of carbon partitioning between M_1 and untransformed austenite at a given partitioning temperature. This model, known as constrained carbon equilibrium (CCE)[13, 14, 15], has two important conditions. The first condition is that competing reactions such as carbide formation and bainite transformation are suppressed. Furthermore, the model assumes a constrained (stationary) interface between austenite and martensite. The endpoint of carbon partitioning is then defined as the point where the chemical potential of carbon is equal between the two phases, i.e. $\mu_c^\alpha = \mu_c^\gamma$ (Figure 2.2). The α/γ interface remains stationary as at the partitioning temperatures used, only long-range diffusion of interstitial atoms can take place, while substitutional atoms remain stationary.

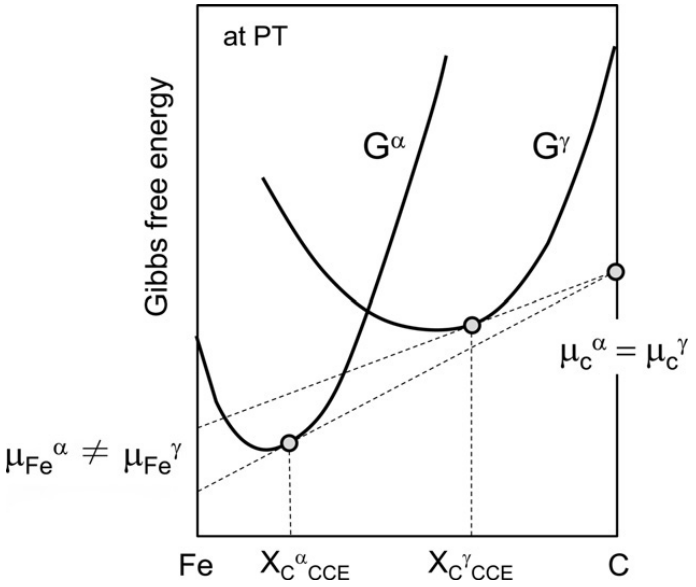

Figure 2.2: Schematic Gibbs free-energy vs. composition diagram showing a a ferrite and austenite composition that satisfies the CCE requirement that the chemical potential of carbon is equal in the two phases. Adapted from [7].

It is reasonable to assume that almost all of the carbon in the alloy partitions into the untransformed austenite if the CCE conditions are realized (full partitioning assumption), because the equilibrium carbon concentration in ferrite is three order of magnitude or less than that in austenite for any given partitioning temperature.[7]

2.2 Competing reactions

In practice, reported volume fractions and carbon content of retained austenite after partitioning and cooling to room temperature are significantly lower than those predicted by the CCE model.[5, 7, 4, 8] This is mainly caused by the occurrence of carbon-consuming reactions such as carbide precipitation during the partitioning step of the Q&P treatment. This leaves less carbon available for the stabilization of austenite through carbon enrichment. Therefore, in order to stabilize the largest volume fraction of austenite and obtain the highest austenite stability, competing reactions such as carbide precipitation, austenite decomposition, and austenite reversion must be minimized.

In martensitic stainless steels, a microstructure free of chromium-rich carbides is also desirable in view of corrosion resistance because the amount of chromium in the matrix remains higher in the absence of chromium-rich precipitates. Mola and De Cooman [4] have shown that stable chromium-rich carbides such as $M_{23}C_6$ and M_7C_3 are unlikely to form at temperatures below 480 °C, due to the low diffusivity of Cr at these temperatures. Therefore, a frequently used partitioning temperature is 450 °C.[16, 4, 5, 7, 8, 17] This temperature allows for carbon enrichment within a short time frame, as would be needed for commercial applications, while being low enough to suppress stable carbide formation and austenite decomposition.[4] Nevertheless, Tsuchiyama et al.[5] reported that less stable M_3C carbides (paraequilibrium cementite) are present in the martensitic regions of Q&P processes AISI 410 martensitic stainless steel after partitioning partitioning at 450°C for 10 minutes.

2.3 Alloying elements

Because carbide precipitation competes with the carbon enrichment of austenite, Q&P steels are typically alloyed with silicon.[2] Silicon is conventionally thought to suppress cementite precipitation, presumably due to its low solubility in cementite and thus the need for silicon to diffuse away from the growing carbide.[18] At temperatures used in Q&P processing the mobility of substitutional atoms is limited, and so the silicon must become trapped in the cementite during its growth. The addition of silicon thereby reduces the free energy change associated with precipitation and leads to a reduction in precipitation kinetics.[19] In stainless steels, however, the high Cr content also contributes to the retardation of cementite precipitation. Therefore, the need for silicon in Q&P processing of martensitic stainless steels has been questioned and both Huang et al.[20] and Tsuchiyama et al.[5] reported that silicon addition does not lead to an increase in austenite stabilization.

Manganese is another alloying element that is often added to Q&P steels to promote the austenite stabilization process. Similarly to Ni, Mn depresses the phase transformation from austenite to ferrite to lower temperatures, i.e. both Ae_1 and Ae_3 are lowered. Both Mn and Cr lower the free energy of austenite relative to that of ferrite, stabilizing the

former and retarding the $\gamma \rightarrow \alpha$ transformation [18].

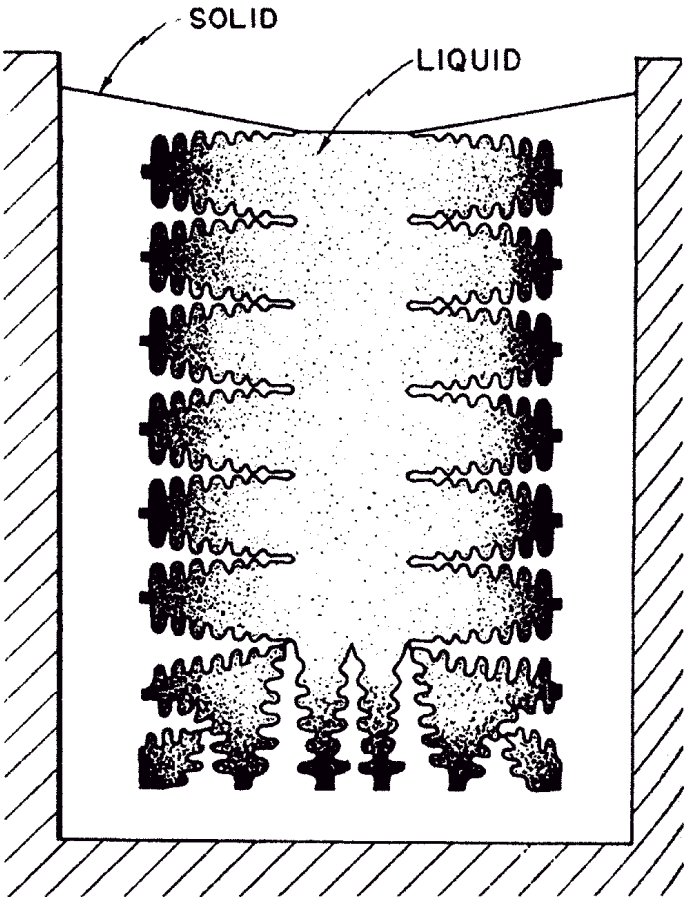

Figure 2.3: Schematic of dendritic solidification. The dark shading in liquid adjacent to dendrites represents concentrations of solute atoms rejected from solid.[21]

Theoretical models that describe the phase transformations in Q&P steels are in principle developed for steels with a homogeneous composition. However, in Mn-rich steels there is a high probability of Mn segregation. Segregation of alloying elements is driven by the difference in elemental solubility between the solid phase forming during solidification and the liquid phase. In the case of Mn-alloyed steels, Mn gets rejected into the interdendritic spaces during solidification (Figure 2.3). Hot rolling causes the interdendritic variations in chemistry to align in bands parallel to the rolling direction, which produces alternating regions of high and low concentrations of solute elements. In other words, the distribution of Mn is homogeneous in the rolling direction (RD), and inhomogeneous in the normal direction (ND).[22] Due to the low diffusivity of Mn, long homogenization treatment must be carried out at high temperatures to obtain a more uniform distribution. However, these treatments are often not economically viable.[18] Moreover, some degree of segregation is almost always present in all types of steel, but this does not always manifest as microstructural banding.[23] To date, limited research has been performed on the effect of elemental segregation on Q&P processing of martensitic stainless steels.

2.4 Mechanical properties of Q&P martensitic stainless steels

The mechanical properties of Q&P processed martensitic stainless steels have been studied extensively by several researchers.[4, 5, 7, 8] The main goal of applying a quenching and partitioning treatment is to obtain an improved combination of strength and ductility compared to other available heat treatments. As can be seen in Figure 2.4, Q&P processing improves the strength-ductility balance considerably compared to conventional quench and tempered (Q&T) AISI 410 martensitic stainless steel. In this particular study, the Q&P processed steel contained 15 vol% retained austenite. The enhanced work hardening rate and increased total elongation can be attributed to the TRIP effect. The occurrence of this phenomenon has been shown by XRD measurements, which showed a decrease in the volume fraction of retained austenite with increasing strain.[7]

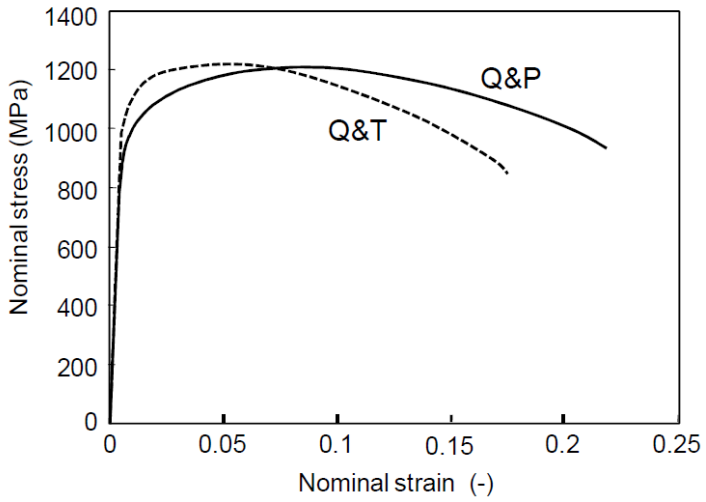

Figure 2.4: Nominal stress-strain curve of 12Cr-0.1C steels with Q&P treatment (P: 450°C-600 s) and Q&T treatment (T: 450°C-120 s).[5]

As was mentioned in section 2.1, different microstructures exist when quenching to a temperature below or above the OQT. These two regimes are clearly visible in the hardness and stress-strain curves of Q&P processed martensitic stainless steels. In regime I (QT<OQT), the microstructure consists of tempered martensite and retained austenite. In regime II (QT>OQT), hard fresh martensite is present as well. As can be seen in Figure 2.5, for similar retained austenite fractions, the Vickers micro-hardness in regime II is significantly higher due to the presence of hard fresh martensite. Figure 2.6 clearly illustrates that the occurrence of fresh martensite results in brittle fracture without any post-uniform elongation. Since the main potential use case of Q&P processed martensitic stainless steels is (automotive) structural applications, brittle fracture is undesirable and so quenching temperatures above OQT should generally be avoided.

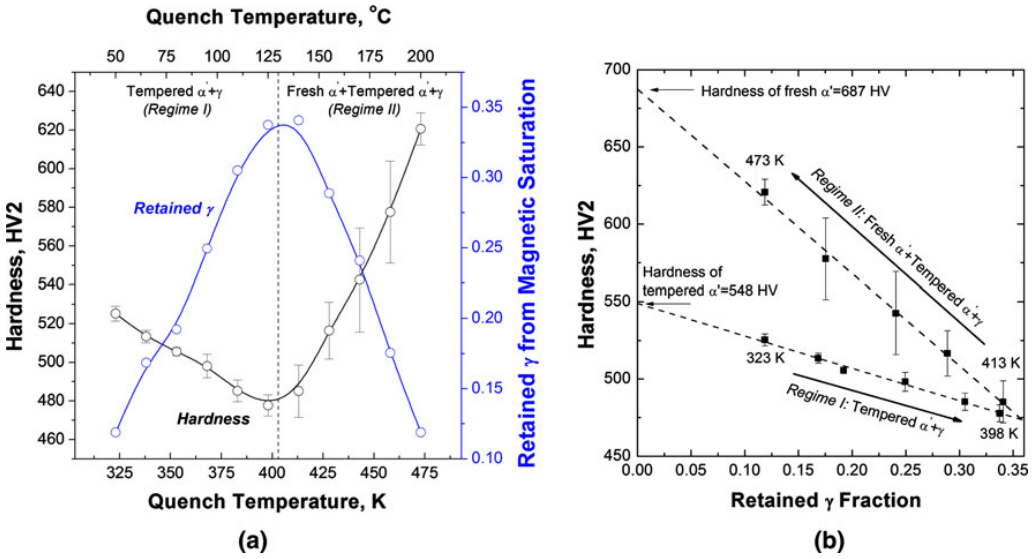

Figure 2.5: (a) Vickers micro-hardness and retained austenite fractions based on magnetic saturation measurements of Q&P specimens. (b) Hardness values in (a) plotted against retained austenite fraction and extrapolated to zero retained austenite fraction.[4]

Although most studies simply focus on maximizing the volume fraction of retained austenite, several researchers have reported that the highest austenite fraction is not necessarily associated with the best combination of strength and ductility.[8] Mola and De Cooman [4] showed that for an AISI 420 stainless steel alloy, the optimal combination of strength and ductility was achieved by quenching to 80 °C (353 K) followed by partitioning at 450 °C (723 K) for 3 minutes (Figure 2.6). After this treatment, the microstructure consisted of 19 vol% retained austenite (measured by saturation magnetization) and the material had a tensile strength of 1570 MPa and total elongation of 15.7 %. However, the quench temperature that resulted in the highest volume fraction of retained austenite (34 vol%) was considerably higher at 140 °C (413 K), but this resulted in a lower austenite stability and inferior mechanical properties.

This demonstrates that the tensile elongation not only depends on the volume fraction of retained austenite, but is also governed by the austenite stability. The mechanical stability of retained austenite is in turn a function of grain size, morphology, and chemical composition. If the austenite stability is too low, it will already transform at low strains, leaving behind large fractions of brittle untempered martensite. Too stable retained austenite, on the other hand, will not transform at all, even at high strains and so the TRIP effect will not be observed. As was demonstrated by Mola and De Cooman [4], the mechanical stability of austenite gradually decreases as QT approaches the OQT. Since high quench temperatures are associated with lower carbon levels in the austenite, chemical stabilization can be seen as the dominant factor determining the mechanical stability of the austenite. Finding the right balance between austenite volume fraction and mechanical stability remains difficult and is mostly based on experimental results.[4, 8]

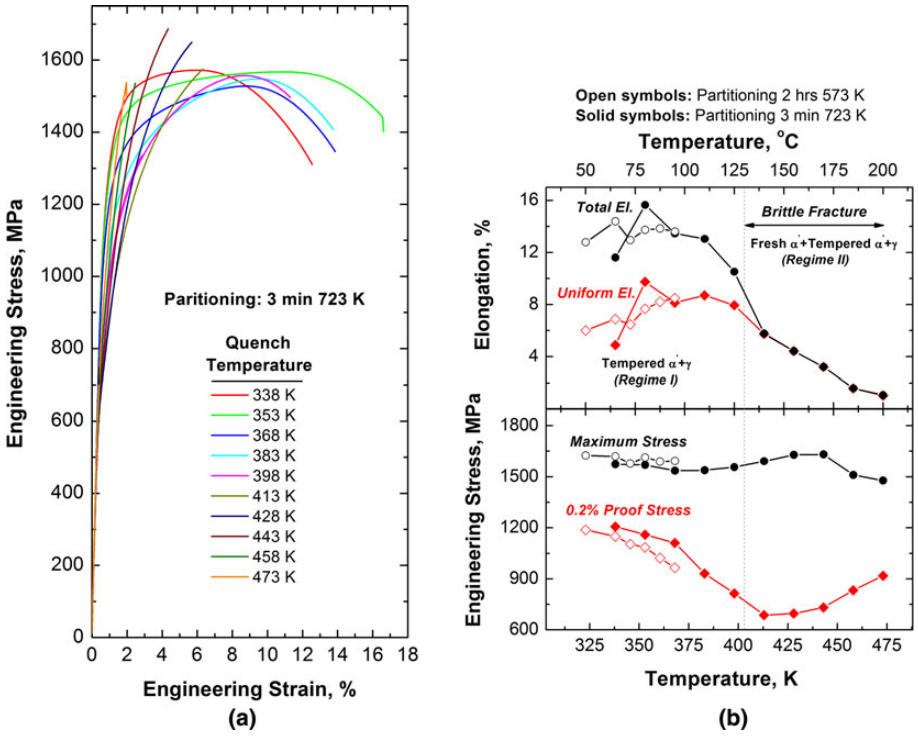

Figure 2.6: (a) Room temperature stress-strain curves for AISI 420 Q&P specimens partition treated at 723 K (450 °C). (b) Summarized tensile properties of Q&P specimens partition treated at 723 K and 573 K (450 °C and 300 °C).[4]

Recent experimental studies [4, 5, 6, 7, 16] have confirmed that Q&P processing is a viable means for creating microstructures containing retained austenite in martensitic stainless steels. Mechanical properties similar to those of other AHSSs have been achieved, showing the potential for Q&P processed martensitic stainless steels in structural applications.[4, 7, 8] However, current research has primarily focused on the Q&P treatment of commercially available AISI 410 and 420 stainless steel grades, so opportunities for composition optimization including microalloying still exist. Unlike other alloying elements such as silicon, the role of manganese in Q&P processing has not yet been studied in detail. In this thesis, the effect of quenching temperature and Mn content on the microstructure development of two novel stainless steel alloys is investigated. This study also aims to investigate the correlation between elemental segregation and the microstructure development of a Q&P processed martensitic stainless steel.

Although predictive models have been developed, finding the optimal processing parameters for Q&P treatments still relies heavily on experimental data. This data, such as the retained austenite phase fraction in Q&P processed specimens, can be acquired with different experimental techniques. However, it has been shown that measurements obtained with methods such as XRD, magnetic saturation and dilatometry are not always in agreement [4, 16]. Therefore, a large number of characterization techniques are utilized and compared in this thesis and a critical view on the reliability of these methods is provided.

Chapter 3

Materials and methodology

This chapter includes detailed descriptions of the experimental methods used to produce the results reported herein. Additionally, the reasoning behind many of the choices made is also explained.

3.1 Production of steel for experimentation

As part of the QPINOX project [11], several new stainless steel compositions were designed considering a target microstructure of tempered martensite and retained austenite after Q&P processing. Other important aspects such as cost of alloying elements, weldability, corrosion resistance, and general processing windows were also considered.

From the designed alloys, several were selected for actual casting and rolling based on the following criteria:

- Suitability and ease for industrial production, including hot/cold rolling and heat treatment equipment.
- Balance between alloys which have good weldability and are more studied in Q&P literature and newer alloys which have limited weldability but potentially very high strength (higher than 1200 MPa UTS).
- A wide range of mechanical properties and microstructures allowing trend analysis between e.g. microstructure and strength, microstructure and corrosion, etc.

The present work focuses on two of the designed alloys, denoted by MedC and MedCMn. The composition of these two alloys is given in Table 3.1. Note that the alloys are identical except for the difference in Mn content and that the cost of alloying elements has been kept low by avoiding additions of Ni and Mo. These alloys provide interesting research opportunities because this specific carbon level (0.2 wt%), as well as manganese addition have not yet been studied in detail in Q&P literature on stainless steels.

Table 3.1: Chemical composition of the studied steels in wt%.

Alloy	**C**	**Si**	**Cr**	**Mn**	**Fe**
MedC	0.20	0.35	12.5	0.7	bal.
MedCMn	0.20	0.35	12.5	3.0	bal.

The selected steel compositions were cast by Acerinox into ingots using vacuum induction melting. After casting, each ingot was homogenized for 3 hours at 1270 °C. The ingots were then hot rolled into slabs of approximately 100 x 20 x 2 cm in 5-7 passes by RINA-CSM (Figure 3.1). The final pass temperature was around 1000 °C. Next, each slab was slowly cooled to room temperature by wrapping them in a ceramic cloth. The realized cooling rate was around 0.1 °C/s. Finally, the plates were annealed for 24 hours at 600 °C. This annealing treatment was intended to reduce the hardness of the plates to allow sample machining but also to mimic the industrial batch annealing process, which is commonly used for 13Cr steel hot-rolled coils.

Figure 3.1: Hot-rolled stainless steel slabs cut in half.

Optical micrographs of the as-received material are presented in Figure 3.2 showing an acicular microstructure.

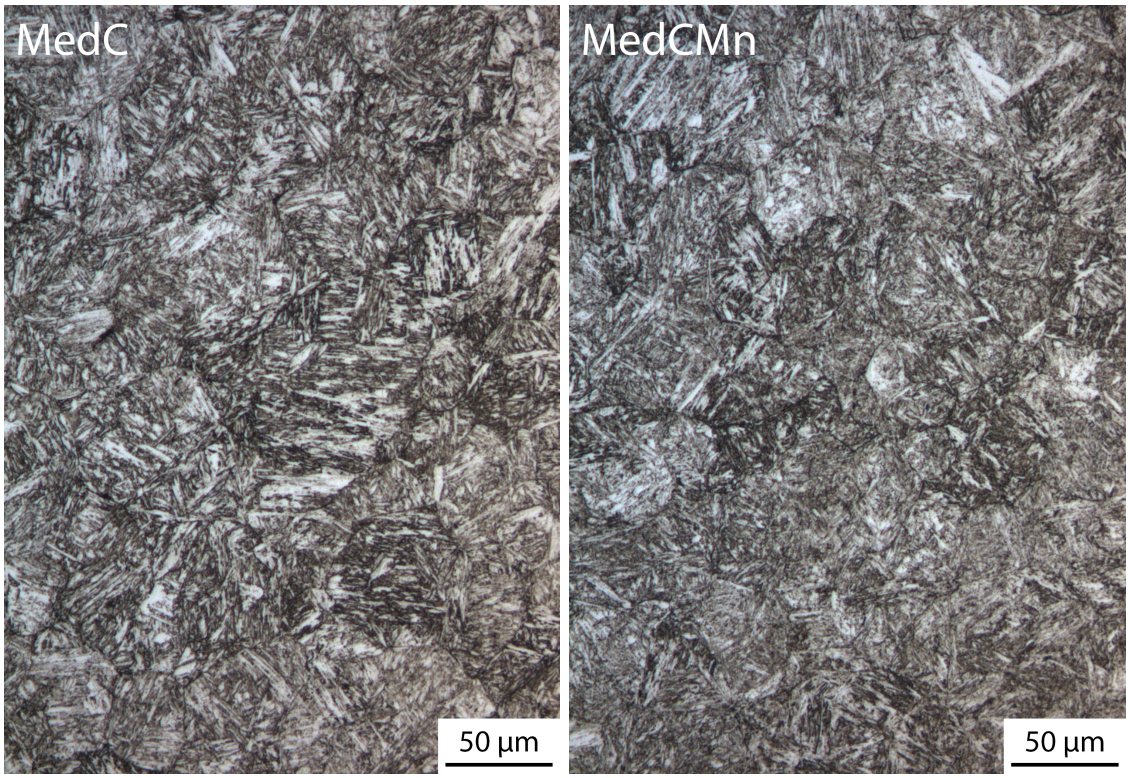

(a) (b)

Figure 3.2: Optical micrographs of the as-received material (a) alloy MedC (b) alloy MedCMn.

3.2 Application of heat treatments by dilatometry

In this study, heat treatments were performed using a dilatometer. Dilatometry is a powerful technique to study solid-state phase transformations because it allows for real-time monitoring of dimensional changes of the material as a function of temperature. When the material undergoes a phase change, e.g. from austenite to martensite, the lattice structure changes and this is in principle accompanied by a change specific volume [24]. By analyzing the relative length change of the sample as a function of temperature, the evolution of the phase transformations and transformation temperatures such as Ac_3 and M_S can be identified.

Cylindrical samples for dilatometry were cut from the hot-rolled slabs using EDM technique (electrical discharge machining). The samples measured 4 mm in diameter and 10 mm in length and were cut with their length parallel to the rolling direction (RD). The sample locations are at around 4 mm below the rolling surface and 60 mm away from the sides to avoid possible center line segregation and decarburization, see Figure 3.3.

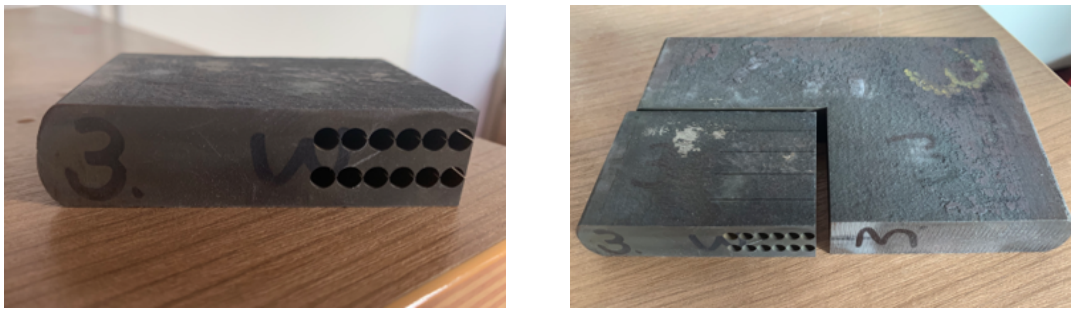

Figure 3.3: Dilatometry sample locations.

The heat treatments were performed using a DIL805 D Bähr/TA Instruments quenching dilatometer, which was programmed with TA Instruments WINTA 10.0 software. The temperature was controlled using an S-type thermocouple spot-welded onto the middle of the cylindrical samples. All samples were induction heated under vacuum and cooled with helium. The dilatometric data was post-processed using Origin 2019 software and Python.

In this work, several types of heat treatments were carried out. To study the kinetics of martensite formation and the change in M_S temperature with cooling rate, specimens were first heated at 10 °C/s to an austenitizing temperature of 1100 °C. After holding for 15 minutes, the specimens were cooled to room temperature with varying cooling rates.

The second type of heat treatment was a complete Q&P cycle as presented in Figure 3.4 with the following processing parameters:

- Heating rate of 10 °C/s for heating to austenitizing temperature and from quenching temperature to partitioning temperature.
- Austenitizing conditions of 1100 °C for 15 minutes.
- Cooling rate of 5 °C/s for cooling to quenching temperature and to room temperature.
- Holding time at quenching temperature of 20 s.
- Partitioning conditions of 450 °C for 5 minutes.

A more detailed description of the various processing parameters and the selection methodology is presented in Section 4.2. The quenching temperature varied per alloy and experiment as will be discussed in Section 4.2.4.

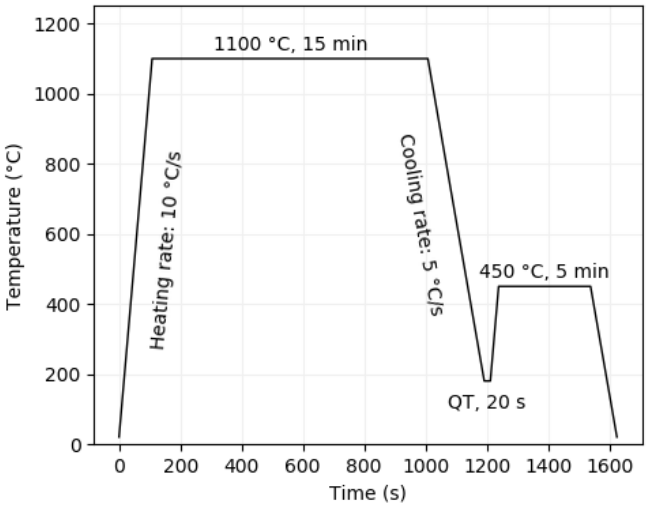

Figure 3.4: Overview of typical Q&P heat treatment used in this study.

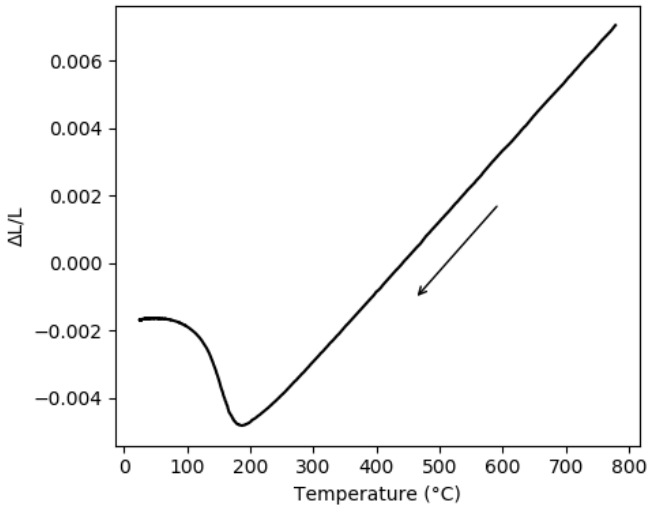

Figure 3.5: Example dilatometric curve showing relative length change associated with martensite formation from austenite during cooling.

Figure 3.5 shows a typical dilatometric curve of martensite formation from austenite during cooling. In this figure, the linear part of the dilatometric curve is regarded as the thermal contraction of the material and the non-linear part is the phase transformation region. To determine the M_S temperature of the two alloys from the dilatometric curves, the strain offset method as described by Yang and Bhadeshia was used [25]. This method defines the first onset of transformation as the point at which a critical strain is achieved relative to the thermal contraction of the parent phase. In this case, the critical strain was calculated for 5 volume percent martensite formation.

The critical strain ϵ_O is calculated using formulae for the lattice parameters of austenite and martensite. The austenite lattice parameter at room temperature (25 °C) can be calculated using Equation 3.1 [26].

$$a_\gamma(nm) = 0.3573 + 0.0033w_C^\gamma + 0.000095w_{Mn}^\gamma - 0.00002w_{Ni}^\gamma + 0.00006w_{Cr}^\gamma \\ +0.00031w_{Mo}^\gamma + 0.00018w_V^\gamma \tag{3.1}$$

where w_i^γ is in weight percent and the composition of austenite as given in Table 3.1 is used. The lattice parameter of martensite can be calculated using a similar formula [27]:

$$a_\alpha(nm) = a_{Fe} + [(a_{Fe} - 0.0279x_C^\alpha)^2(a_{Fe} + 0.2496x_C^\alpha) - a_{Fe}^3]/(3a_{Fe}^2) - 0.003x_{Si}^\alpha \\ +0.006x_{Mn}^\alpha + 0.007x_{Ni}^\alpha + 0.031x_{Mo}^\alpha + 0.005x_{Cr}^\alpha + 0.0096x_V^\alpha \tag{3.2}$$

where x_i^α represents the mole fraction of alloying element i in phase α and $a_{Fe} = 0.28664$ nm is the lattice parameter of pure iron at room temperature.

The critical offset strain ϵ_O corresponding to a specific volume fraction of martensite V is then calculated using Equation 3.3:

$$\epsilon_O = \{a_\gamma^{-3}[2Va_\alpha^3 + (1-V)a_\gamma^3]\}^{1/3} - 1 \tag{3.3}$$

An example illustrating the offset method is given in Figure 3.6. A linear regression line is fitted to the thermal contraction data of the austenite and offset with the critical strain ϵ_O. For all dilatometry experiments, fitting was performed to the straight section of the cooling curve at temperatures below 800 °C. At higher temperatures, at the beginning of quenching/cooling, considerable thermal inaccuracies can be observed. These could be attributed to vibrations caused by the impinging flow of the cooling gas and thermal gradients within the specimen (Figure 3.7).

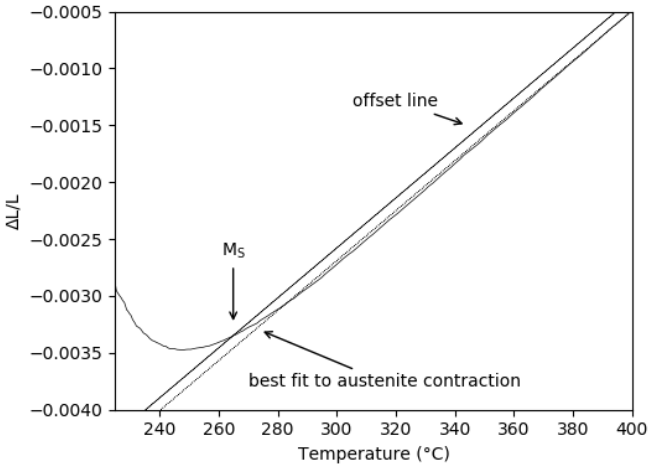

Figure 3.6: Offset method illustrated for MedC specimen quenched to room temperature.

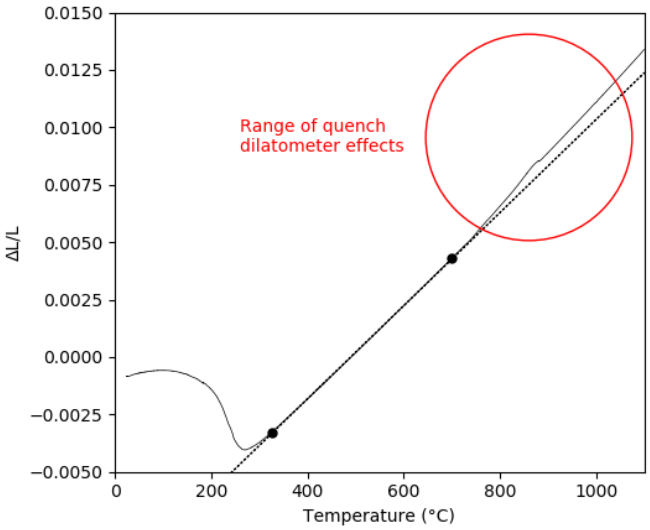

Figure 3.7: Thermal inaccuracies at the beginning of cooling to room temperature of a MedC specimen with a cooling rate of 10 °C/s. Fitting range is indicated by • dots.

3.3 Optical microscopy

After the samples were subjected to a heat treatment using the dilatometer, the samples were cut in half so they could be studied using optical microscopy, X-ray diffraction, electron backscatter diffraction and electron probe micro analysis. Cutting was performed using a Struers Minitom low-speed cutting machine with a 0.5 mm thick water-cooled abrasive cut-off wheel. Rotational speed was set at 100 - 200 rpm. This cutting method was selected because it produces minimal heat and does not cause deformation of the samples during cutting. This is important to preserve the microstructure obtained at the end of the heat treatment. After sectioning, the specimens measured 4 to 5 mm in length and 4 mm in diameter (Figure 3.8b).

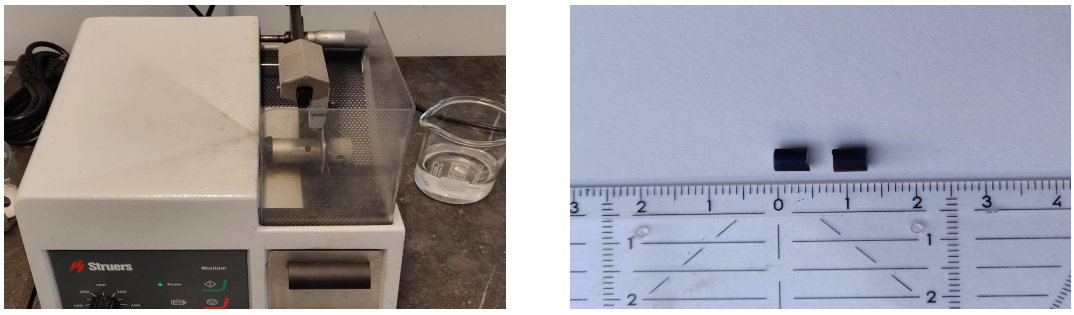

(a) (b)

Figure 3.8: (a) Samples being cut on Struers Minitom gravity-fed cutting machine. (b) Samples cut in half.

The cut faces of the heat-treated samples were then ground and polished. Special sample holders were made to hold the relatively short specimens securely during the grinding and polishing process (Figure 3.9). Approximately 0.5 mm of the material was removed using course silicon carbide (SiC) paper with water as lubrication. Wet grinding was then

continued using progressively finer grit silicon carbide paper, finishing with p2000 grit. This was followed by polishing using polishing cloths loaded with 3 µm and 1 µm diamond polishing abrasive in liquid suspension.

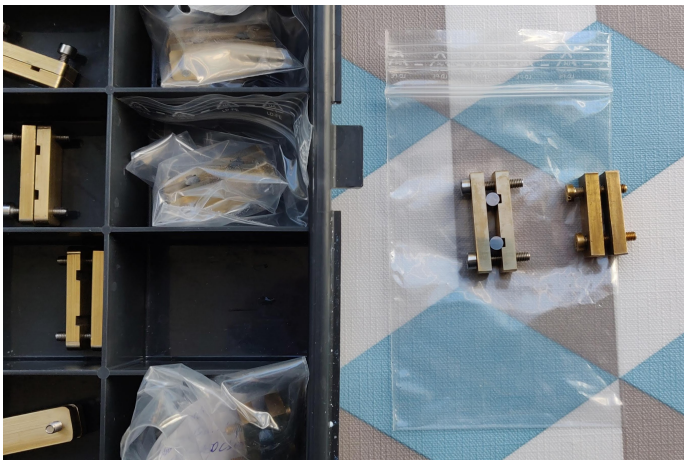

Figure 3.9: Two cylindrical samples held in custom sample holder used for grinding and polishing.

After polishing, the samples were etched using Vilella's reagent. This etchant is listed in ASTM standard E 407 as formula number 80 [28]. The composition of this etchant is given in Table 3.2. Samples were swabbed or submersed in etchant for 30 to 90 seconds.

Table 3.2: Composition of Vilella's reagent (ASTM E 407 formula 80 [28]).

Chemical name	**Concentration**
Hydrochloric acid	5 mL
Picric acid	1 g
Ethanol (95%) or methanol (95%)	100 mL

3.4 Electron microscopy

3.4.1 Electron backscatter diffraction (EBSD)

Electron backscatter diffraction (EBSD) was used to investigate the crystallographic orientation and phase distribution of the resulting microstructure after Q&P treatment. Samples were prepared in the same way as for optical microscopy with an additional polishing step. For EBSD measurements, surface preparation is critical because diffracted electrons only escape from within a few tens of nanometers below the sample surface [29]. Therefore, an additional final polishing step was performed using 0.04 µm colloidal silica suspension (Struers OP-S NonDry) on an MD-Chem polishing cloth. Colloidal silica is a chemo-mechanical polish that combines the effect of mechanical polishing with etching which produces an excellent surface finish for EBSD analysis. Samples were polished for 20 minutes by hand.

EBSD patterns were acquired using a scanning electron microscope by means of the Flamenco Oxford-HKL system. The analysis was performed with an acceleration voltage

of 20 kV and a step size of 100 or 50 nm. This resulted in an overall index rate of 40-65% (Figure 3.10).

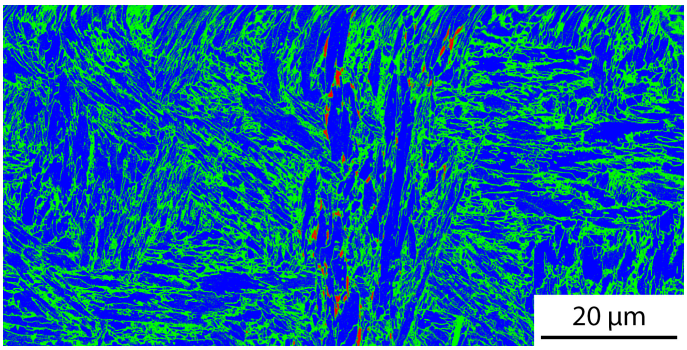

Figure 3.10: EBSD phase map of a MedCMn sample with an index rate of 63 %. Red, blue and green pixels indicate FCC, BCC, and zero solutions respectively.

The EBSD orientation data was post-processed using Channel 5 Tango software. A standard noise reduction routine was performed to remove points that could not be indexed. First, a single "1-neighbour zero solution" extrapolation step was performed for the FCC phase only. Next, "4-neighbour zero solution" extrapolation was performed for both phases until there were no zero solutions left.

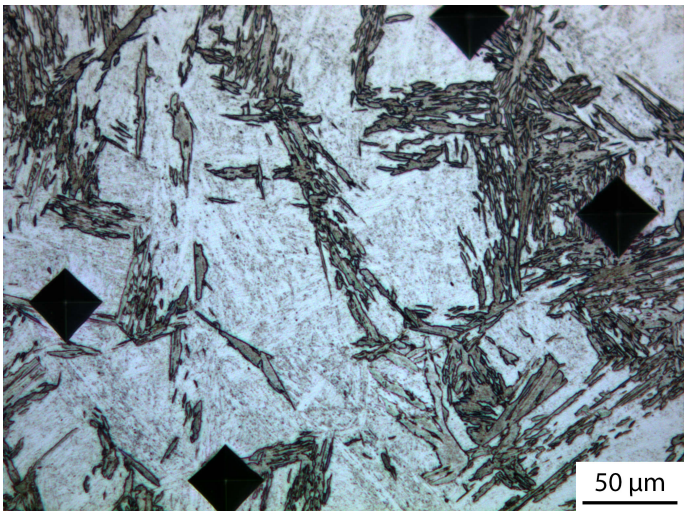

Figure 3.11: Example of indented etched dilatometry specimen. Indents were placed using a square-based pyramid diamond indenter with an angle of 136 degrees between faces and an applied load of 0.5 kgf (HV0.5).

To compare optical micrographs with EBSD scans of the same sample area, an analysis area was marked by indents using a microhardness testing machine. Markings were placed roughly 2.5x the indent diameter away from the scanning area. After indenting the etched specimens, the etched surface was repolished with a 1 µm polishing suspension and OP-S to prepare the surface for EBSD without removing the indents completely. Under the SEM, the indents could then be used to align the specimen and to select the scanning area.

3.4.2 Electron probe micro analysis (EPMA)

Qualitative and quantitative analysis of alloying element distribution was performed using electron probe micro analysis (EPMA). First, two line scans were executed to obtain accurate composition data along the normal direction (ND) of the studied specimen. Next, a compositional mapping was performed to obtain the elemental distribution of C, Si, Cr, and Mn in the marked analysis area. Within this area marked by indents, an EBSD scan had been performed prior to EPMA analysis.

The measurements were performed with a JEOL JXA 8900R microprobe using an electron beam energy of 10 keV and beam current of 50 nA employing wavelength dispersive spectrometry (WDS). The composition at each analysis location was determined using X-ray intensities of the constituent elements after background correction relative to the corresponding intensities of reference materials. The obtained intensity ratios were then processed with the matrix correction program CITZAF. [30] The line scans were performed with a step size of 2 µm and involved the elements C, Si, Cr, and Mn, where Fe was obtained by difference. The energy of the spectral lines, detection limit and counting error is given in Table 3.3.

Table 3.3: Energy (keV), detection limit (ppm), and counting error (wt%) for each of the elements analyzed using WDS.

Element, X-ray line	Energy (keV)	Detection limit (ppm)	Counting error (wt%)
Carbon, C Kα	0.282	50	0.15
Silicon, Si Kα	1.740	15	0.03
Chromium, Cr Kα	5.474	50	0.20
Manganese, Mn Kα	5.898	50	0.20

Qualitative elemental distribution mapping of C, Si, Cr, and Mn was performed using a 10 keV electron beam energy and 200 nA beam current. An air jet was used to suppress the contamination of the sample surface with carbon.

3.5 X-ray diffraction measurements (XRD)

X-ray diffraction was used to investigate the phase fractions and austenite lattice parameter of the heat-treated samples. Heat-treated dilatometry specimens were cut in half and then ground and polished up to 1 µm diamond suspension. It is well known that retained austenite may transform into martensite when a certain amount of stress or strain is applied. Hence, the ASTM E975 – 13 standard [31] reports that great care should be taken when preparing samples for X-ray diffraction measurement of retained austenite fraction, as not to induce transformation of austenite to martensite. For this reason, slow rotational speed and light contact pressure were used during the grinding and polishing process to minimize the mechanically-induced transformation of retained austenite. The influence of sample preparation on XRD measurement of retained austenite fraction is further discussed in Section 4.4

The XRD experiments were carried out by the X-ray facilities group of the Materials Science and Engineering department at Delft University of Technology. In the first set of

experiments, the retained austenite fraction after direct quenching to room temperature with a cooling rate of 5 °C/s was determined using a Bruker D8 Discover diffractometer equipped with an Eiger-2 500k 2D-detector and Cu Kα radiation. The diffractometer was operated with an acceleration voltage of 50 kV and a current of 1000 µA. The scanning range of 2θ was 30° – 140° with a step size of 0.040° 2θ. The samples were mounted on a Si510 wafer in a standard sample holder (Figure 3.12).

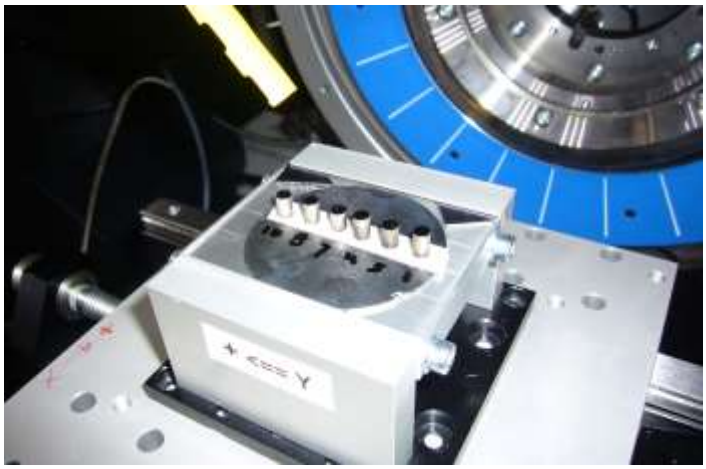

Figure 3.12: Cylindrical samples with polished top surface fixed on a Si510 wafer in a standard sample holder.

From the measured patterns using this diffractometer, semi-quantification was not possible. Therefore, for the samples that showed some austenite content, measurements were repeated using another type diffractometer using Co Kα radiation and sample spinning. This diffractometer was also used for all subsequent measurements. The main advantage of using Co radiation is the higher penetration depth.

The second set of diffraction experiments were performed using a Bruker D8 Advance diffractometer with Bragg-Brentano geometry, graphite monochromator, and Vantec position sensitive detector using Co Kα radiation. Typical operating parameters were as follows: acceleration voltage of 45 kV, current of 35 mA, and spinning speed of 30 rpm. Samples were mounted on a SD52 holder with some plasticine (Figure 3.13). The measurements consisted of a coupled θ - 2θ scan from 40° - 130° with a step size of 0.034° 2θ and a counting time of 2 s per step.

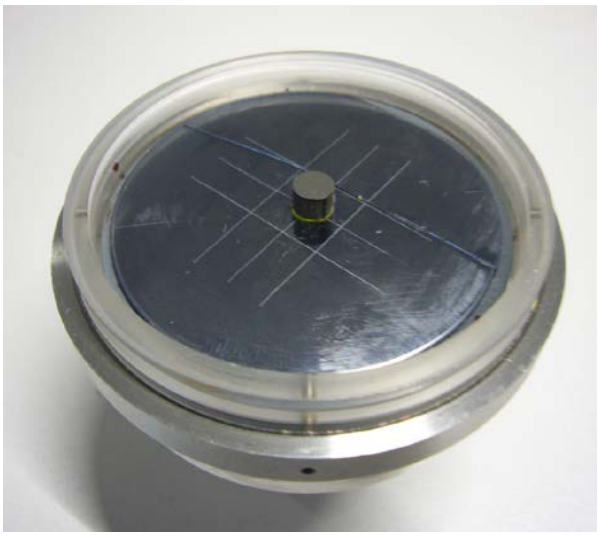

Figure 3.13: Cylindrical samples mounted on SD52 holder using plasticine.

A series of measured XRD patterns is shown in Figure 3.14 (offset vertically). From these patterns, the austenite content in the samples was calculated by comparing the areas under the ferrite peaks {110}, {200}, {200}, and {200} with the areas under the austenite peaks {111}, {200}, {220}, and {311} [32].

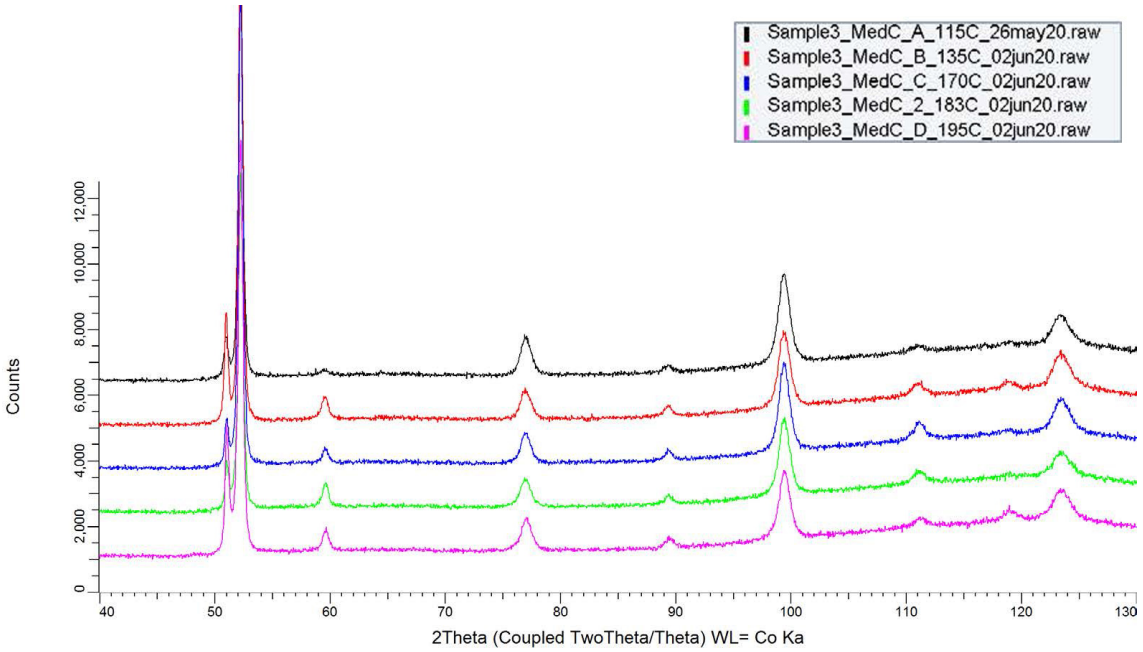

Figure 3.14: Typical XRD patterns of several samples

The fraction of austenite was calculated as follows by assuming that the sample consists of two phases: austenite and ferrite (ignoring the presence of carbides):

$$f_\gamma = \frac{I_\gamma}{I_\alpha + I_\gamma} \tag{3.4}$$

where I_γ and I_α are the average normalized peak intensities of the austenite and ferrite

peaks respectively:

$$I_\gamma = \frac{1}{n} \sum_{1}^{n} \left(\frac{I_{\gamma hkl}}{R_{\gamma hkl}} \right) \tag{3.5}$$

In Equation 3.5, n is the number of austenite peaks, $R_{\gamma hkl}$ is the calculated intensity of a particular {hkl} austenite peak taken from [32], and $I_{\gamma hkl}$ is the measured intensity of a particular {hkl} austenite peak above the background. The average normalized intensity of the ferrite peaks is calculated in an analog way.

Because an auto divergence slit is used, the irradiated area remains constant throughout the whole scanning range. However, this means that with increasing 2θ, the specimen receives a larger part of the incoming beam. In other words, the received and diffracted intensity increases with 2θ and so the area under the peaks increases. The R-values taken from [32] do not include this effect as a fixed divergence slit is assumed. Therefore, to calculate the austenite fraction correctly, the R-values are modified by multiplying them with $\sin(\theta)$, see Table 3.4.

Table 3.4: Standard and modified R-values for reflection peaks of ferrite and austenite. Standard values are taken from [32] for cobalt radiation and austenite with 0.2 wt% C.

Reflection peak	$\alpha_{\{110\}}$	$\alpha_{\{200\}}$	$\alpha_{\{211\}}$	$\alpha_{\{220\}}$	$\gamma_{\{111\}}$	$\gamma_{\{200\}}$	$\gamma_{\{220\}}$	$\gamma_{\{311\}}$
R 0.2 C	115.3	14.8	32.4	15.4	90.4	39.2	21.6	31.9
R 0.2 C $\sin(\theta)$	50.9	9.2	24.8	13.6	39.0	19.5	15.2	26.3

Diffraction data was analysed using Bruker DIFFRAC.EVA V5.2 software. As can be seen in Figure 3.14, the {111} austenite peak overlaps with the {110} ferrite peak which makes it difficult to determine the area under the peaks accurately. First, the area of the {111} austenite and {110} ferrite peak together was determined. Then, the area of the {111} austenite peak was approximated using a linear background and subtracting it from the total area (Figure 3.15). Note that this gives a slight under-estimation of the {111} austenite peak area and an over-estimation of the {110} ferrite peak area. For this reason, the austenite fraction was also determined without the {110} and {111} peak.

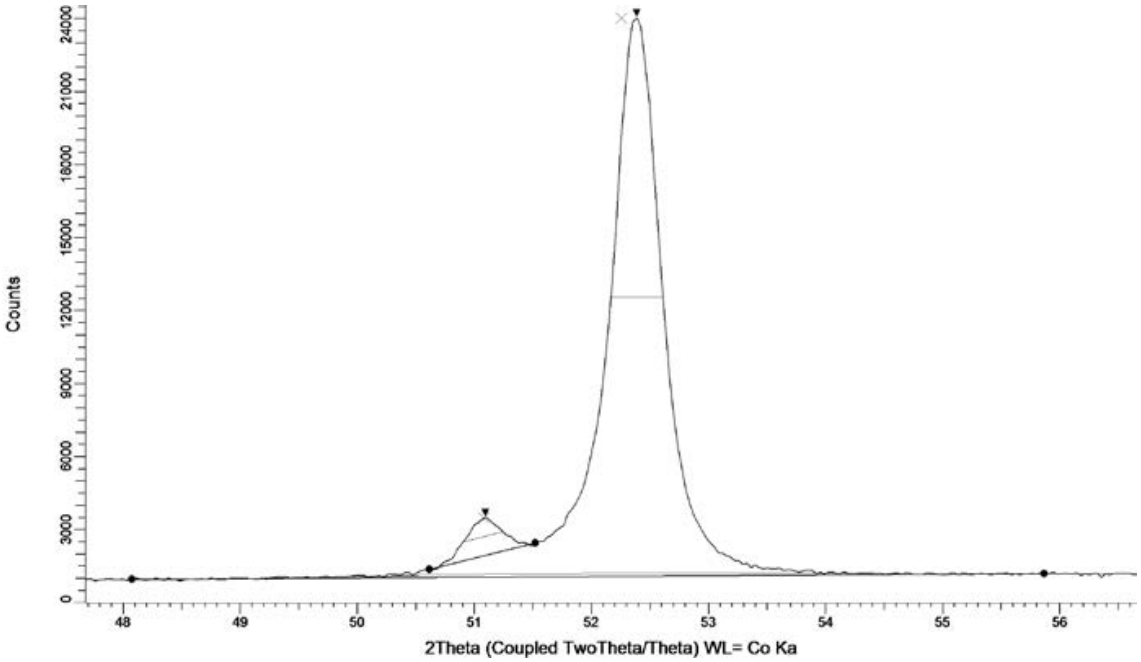

Figure 3.15: Example of estimating the areas of overlapping austenite (left) and ferrite (right) peaks.

X-ray diffraction was also used to measure the austenite lattice parameter. The interplanar spacing d_{hkl} corresponding to a particular {hkl} peak can be determined using the well known Bragg equation:

$$n\lambda = 2d_{hkl}\sin\theta \tag{3.6}$$

where n is the order of reflection, λ is the wavelength of the radiation, and d_{hkl} is the lattice plane spacing. θ is the reflection angle corresponding to a particular {hkl} peak as determined by the DIFFRAC.EVA software.

For cubic crystals, the lattice spacing a can be obtained from the interplanar spacing d through the following relation:

$$a_{hkl} = d_{hkl}\sqrt{h^2 + k^2 + l^2} \tag{3.7}$$

where a_{hkl} is the lattice parameter and h, k, and l are the Miller indices of the lattice plane. Although it is possible to determine the austenite lattice parameter using only one austenite reflection peak, more accurate results can be obtained by taking the average of multiple peaks or by applying Cohen's method, e.g. as described by Garcia-Mateo et al.[33, 34].

With this method, the austenite lattice parameters as determined from the individual peaks are plotted against $cos^2(\theta)/sin(\theta)$, and the precise lattice parameter is obtained by extrapolating the diffraction angle θ to 90°, with the highest diffraction angles being given the greatest weights in the extrapolation. For this, a linear regression line is plotted through a data set containing just one point for the lowest θ value, two identical points for the next θ value and so on. This is done because the highest θ values are associated with

smaller errors in the calculated lattice parameter (stemming from the $sin(\theta)$ in the Bragg law) [34]. In this thesis, the precise lattice parameter was determined using both Cohen's method and the average of multiple reflection peaks to compare the two methods.

From the determined austenite lattice parameter, the austenite carbon content can be estimated using the following empirical relationship [35]:

$$\begin{aligned} a_{fcc} = 3.5780 + 0.033x_C + 0.00095x_{Mn} - 0.0002x_{Ni} + 0.0006x_{Cr} \\ +0.0056x_{Al} + 0.0031x_{Mo} + 0.0018x_V \end{aligned} \tag{3.8}$$

where a_{fcc} is the austenite lattice parameter in ångström and x_i corresponds to the weight percent of elements "i" in austenite.

It is reasonable to assume that carbon is the only element responsible for the variations in lattice parameter, because the substitutional atoms diffuse very slowly at the partitioning temperatures used in Q&P processing. Thus for the other elements, the base composition (Table 3.1) is assumed. Possible effects of internal stresses on the lattice parameter were ignored.

Chapter 4

Results

4.1 Theoretical study of the alloys

Prior to starting this thesis, thermodynamic calculations were performed for the designed alloys with Thermo-Calc Software (2019b, TCFE9.1 database) to predict phase stabilities and critical temperatures. The phase diagrams in terms of mass fraction (BPW(*)) versus temperature for alloy MedC and MedCMn are shown in Figure 4.1.

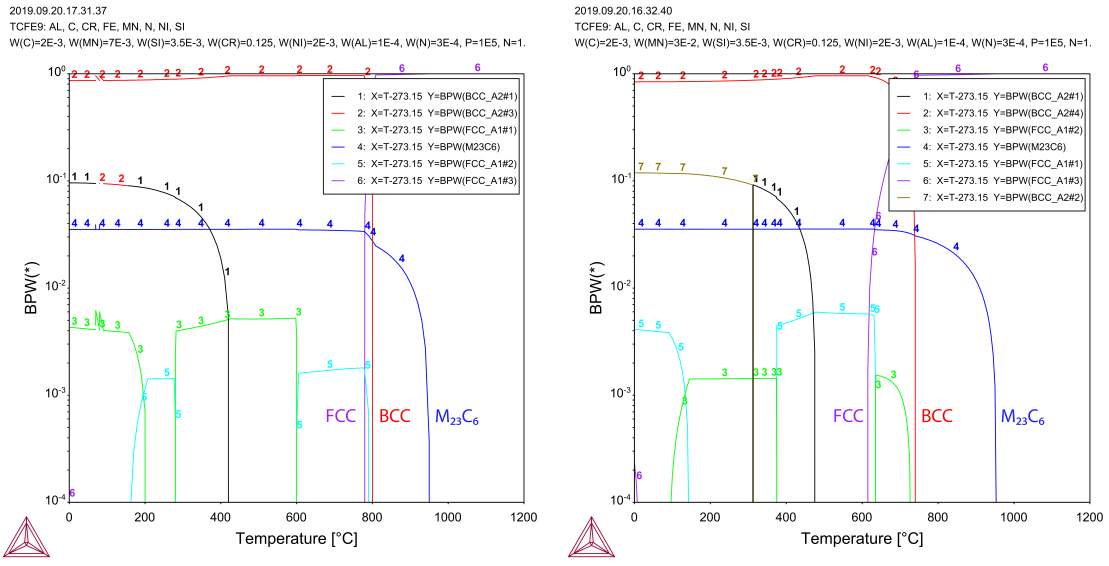

(a) (b)

Figure 4.1: Phase mass fraction (BPW(*)) versus temperature for (a) alloy MedC and (b) alloy MedCMn [11].

In the phase diagrams, the phases that are relevant for the studied compositions and can occur in reality in martensitic stainless steels are: ferrite (BCC_A2#3), austenite (FCC_A1#3) and chromium-rich carbides (M23C6). The other phases shown in the diagrams were found to be intermetallic compounds that do not occur in martensitic stainless steels.[11]

From these diagrams, it can be seen that considering thermodynamic equilibrium,

at low temperatures (below around 600 °C) the stable phases in both alloys are ferrite and chromium-rich $M_{23}C_6$ carbides. Above the Ae_1 temperature (around 600-800 °C) separating the $\alpha + \gamma$ and α phase fields for a specific alloy, austenite is also present and the ferrite phase fraction decreases. Above the Ae_3 temperature (around 750-800 °C) separating the $\alpha + \gamma$ and γ phase fields, the ferrite fraction is zero and the only stable phases are austenite and $M_{23}C_6$. The complete dissolution of $M_{23}C_6$ particles occurs at temperatures above 950 °C, leaving only austenite. This temperature (denoted by T_γ) is of primary importance for selecting suitable austenitizing conditions, as will be discussed in Section 4.2.1.

From Figure 4.1, the Ae_1, Ae_3 and T_γ temperatures were extracted. The values are reported in Table 4.1.

Table 4.1: Thermo-Calc predictions for Ae_1, Ae_3 and T_γ.

Alloy	**Ae_1 (°C)**	**Ae_3 (°C)**	**T_γ (°C)**
MedC	778	800	952
MedCMn	614	740	955

As can be seen from these values, the Ae_1 temperature is significantly reduced by Mn addition. This is in qualitative agreement with published empirical formulations for Ae_1 such as those by Tricot and Castro [36]. Thermo-Calc also predicts a lower Ae_3 with increasing Mn concentration. The T_γ temperature, defined as the minimum temperature at which only austenite exists (no carbides at all), is almost identical for the two alloys. While the effect of Mn addition is minimal, it was found that T_γ significantly increases with C addition due to increasing $M_{23}C_6$ precipitate stability.

Besides the Thermo-Calc analysis to predict Ae_1, Ae_3 and T_γ, an empirical approach was used to obtain an equation for the martensite-start temperature. Fitting to experimental data from literature studies on Q&P processing of 13Cr martensitic stainless steels [4, 6, 7, 8, 37, 38] resulted in the following equation [11]:

$$M_S(^\circ C) = 553.7 - 530.8w_C - 9.7w_{Si} - 12.1w_{Cr} - 30.4w_{Mn} \tag{4.1}$$

where w_i represents the concentration in weight percent of the elements identified by the subscript. The coefficients for Mn and Cr are taken from the well known Andrews equation [39] which was validated by Kung and Rayment [40] for steels with up to 12 wt% Cr and 5 wt% Mn. The M_S temperatures of alloys MedC and MedCMn as calculated using Equation 4.1 are reported in Table 4.2.

Table 4.2: M_S temperature for alloy MedC and MedCMn as calculated using Equation 4.1

Alloy	**C (wt%)**	**Si (wt%)**	**Cr (wt%)**	**Mn (wt%)**	**M_S (°C)**
MedC	0.2	0.35	12.5	0.7	272
MedCMn	0.2	0.35	12.5	3.0	202

4.2 Design of the heat treatments

Several preliminary experiments were performed to determine suitable processing parameters (e.g. cooling rate and austenitizing conditions) for the Q&P treatment of both alloys. In the section below, a detailed description of these experiments is given and the methodology for selecting the process parameters is explained.

4.2.1 Selection of austenitizing conditions

The Q&P treatment starts with an austenitization step for which two parameters needed to be selected, namely time and temperature. Since the stabilization of untransformed austenite via carbon enrichment is dependent on the availability of carbon during partitioning, it is important that the carbon is not locked up in carbides that have had insufficient time or temperature to dissolve completely during the austenitization stage. Hence, the main goal of the austenitization step is to homogenize the material and to ensure that all pre-existing Cr-rich carbides such as $M_{23}C_6$ dissolve.

The progressive dissolution of Cr-carbides at elevated temperatures raises the concentration of carbon and chromium in solid solution, which lowers the M_S temperature. The austenitizing conditions that result in complete dissolution of these carbides can therefore be studied experimentally using dilatometry by measuring the associated decrease in M_S temperature during cooling from austenitizing temperature. This has already been demonstrated in several studies [41, 17, 8, 20] which report that for the commercial martensitic stainless steel grade AISI 420, complete dissolution of the Cr-rich carbides occurs at an austenitizing temperature of 1180 °C. However, in literature, greatly varying austenitizing treatments are reported for Q&P processing of martensitic stainless steels, ranging from 30 minutes at 1000 °C [7] to 2 minutes at 1250 °C [8].

For selecting suitable austenitizing conditions, several experiments were carried out by G. Li, one of the QPINOX project researchers. One of the designed alloys, with composition 0.13C-0.7Mn-0.35Si-12.0Cr, was subjected to a series of dilatometry experiments with varying austenitizing conditions. Table 4.3 shows that the M_S temperature decreased with longer holding times, indicating the gradual dissolution of Cr-rich carbides. Austenitizing at 1200 °C for 10 minutes or at 1100 °C for 15 minutes resulted in an M_S temperature close to the theoretical M_S temperature that was calculated using Equation 4.1.

Table 4.3: Martensite start temperature of QPINOX alloy with composition 0.13C-0.7Mn-0.35Si-12.0Cr subjected to various austenitizing conditions [11].

Austenitizing conditions	**1200 °C 3 min**	**1200 °C 5 min**	**1200 °C 10 min**	**1100 °C 15 min**	**Equation 4.1**
M_S (°C)	327	350	320	317	315

From a production economics point of view, the time taken for the austenitizing step is also an important consideration. Excessively long heat treatments are costly and should therefore be avoided. Generally speaking, a slightly higher austenitizing temperature has a far greater effect on accomplishing complete austenitization and dissolution of carbides than longer hold times at some lower temperature [42]. Thus, a shorter austenitizing hold time at 1200 °C would be preferred over a longer hold time at 1100 °C. However, in

the present study, the selection of the austenitizing conditions was also influenced by the available dilatometry equipment.

The use of alumina (Al_2O_3) push-rods caused serious measurement errors at the onset of quenching which was most likely related to the impinging flow of cooling gas. Also, non-linear thermal contraction was only observed when using alumina push-rods. Therefore, fused silica push-rods were used instead. These push-rods did not cause measurement errors, but their maximum operating temperature is limited to 1100 °C. Because austenitizing at 1100 °C resulted in a similar M_S temperature as austenitizing at 1200 °C (see Table 4.3), austenitizing conditions of 1100 °C for 15 minutes were used for the rest of the experiments, allowing the use of fused silica push-rods.

Note that this detailed analysis was only performed for one of the designed QPINOX alloys. For all other alloys, the same austenitizing conditions were used. According to the thermodynamic model as presented in Section 4.1, these conditions should also lead to full dissolution of precipitates in the alloys used for this study.

4.2.2 Selection of cooling rate

The cooling rate for cooling from austenitizing temperature to QT needs to be high enough to achieve a martensitic structure and to prevent unwanted reactions such as ferrite or pearlite formation. To select a suitable cooling rate, samples of both alloys were subjected to a series of dilatometry experiments consisting of austenitizing at 1100 °C for 15 minutes, followed by continuous cooling to RT with cooling rates of 1 °C/s, 5 °C/s, 10 °C/s, 20 °C/s, and quench. The resulting dilatometry curves are shown in Figure 4.2.

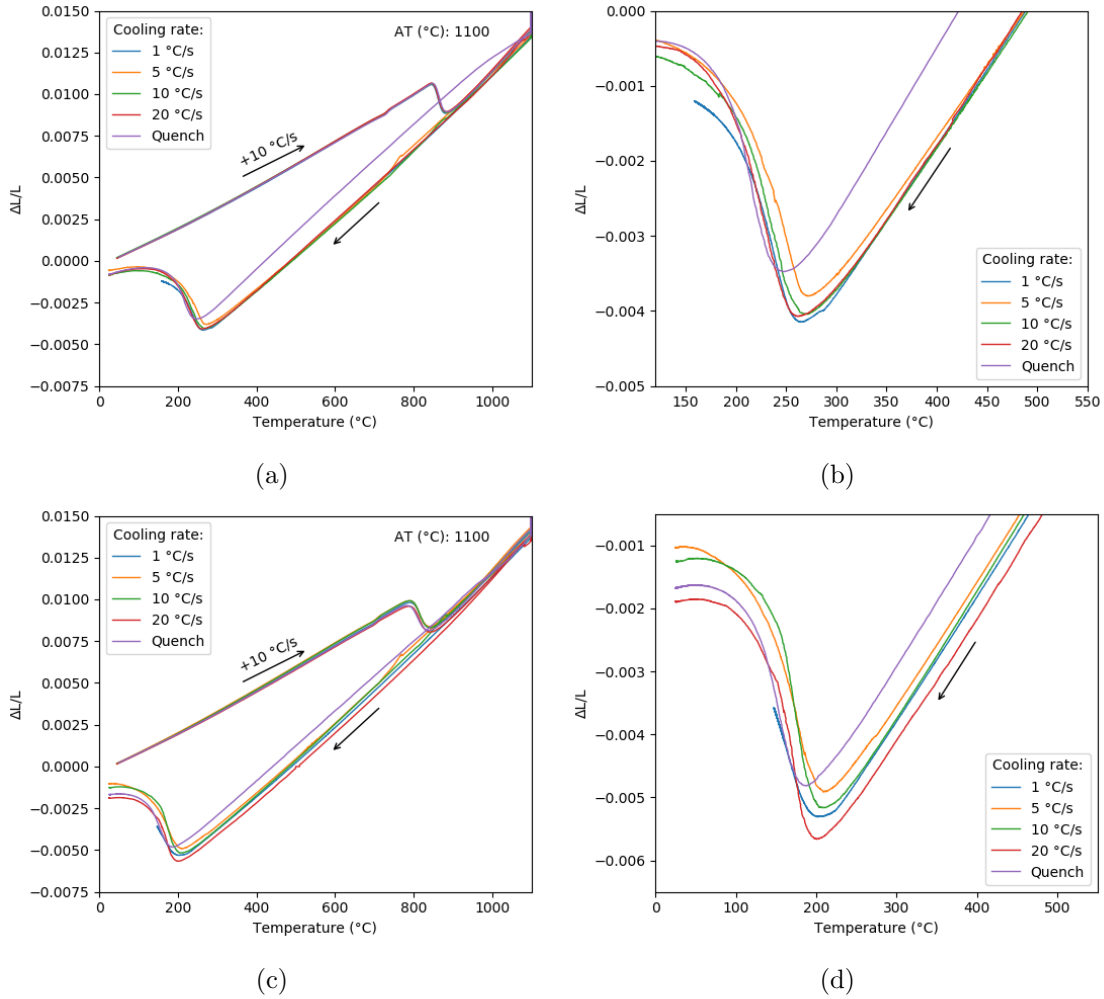

Figure 4.2: Relative length changes of dilatometry specimens austenitized at 1100 °C for 15 minutes followed by continuous cooling to room temperature with different cooling rates. (a), (b) alloy MedC, and (c), (d) alloy MedCMn.

The M_S temperatures corresponding to 5 vol% martensite formation as determined using the offset method (see Section 3.2) are reported in Table 4.4.

Table 4.4: M_S temperatures for different cooling rates as determined using the offset method with ϵ_O corresponding to 5 vol% martensite formation.

	1 °C/s	**5 °C/s**	**10 °C/s**	**20 °C/s**	**Quench**
MedC	261 °C	268 °C	264 °C	264 °C	241 °C
MedCMn	204 °C	211 °C	211 °C	203 °C	185 °C

Except for the highest cooling rate, only small differences in M_S can be observed. Yang and Bhadeshia [25] report an uncertainty of about ± 12 °C in the martensite start temperature when using the offset method, so the differences in M_S can (partially) be attributed to measurement errors. Figures 4.2b and 4.2d also show that the onset of martensite transformation is not well defined. This is also known as the 'slow start' phenomenon, which can lead to a significant overestimation of M_S [43]. This phenomenon is most likely caused by experimental conditions such as a non-uniform temperature of the samples during cooling. Besides this, another possible factor that can explain the

'slow start' effect and observed variations in M_S is material variability in grain size and composition, both within an individual specimen and between specimens of the same alloy.

Because alloys MedC and MedCMn did not show a significant change in M_S temperature with cooling rate in the range of 1 to 20 °C/s, the results from the other QPINOX alloys were also considered. Because two of the alloys showed a significant change in M_S temperature for the lowest cooling rate, it was decided to use a cooling rate of 5 °C/s for the rest of the experiments. This cooling rate is low enough to allow for precise control of the quenching step and high enough to prevent unwanted reactions during cooling. Furthermore, it falls within the cooling rate acceptable for industrial processing, which is limited to 10 °C/s for microstructure control [11].

4.2.3 Martensite kinetics

To control the fraction of primary martensite that forms during Q&P processing, the kinetics of martensite transformation need to be known. Martensite formation is usually described as an athermal reaction where the fraction transformed depends on the undercooling below M_S.[18] Probably the most widely used model to describe the progress of martensitic transformation is the Koistinen-Marburger equation [44]:

$$f_{M_1} = 1 - \exp[-\alpha_m \cdot (M_S - QT)]; \quad M_S > QT > -80°C \tag{4.2}$$

where f_{M_1} represent the volume fraction of primary martensite that forms by quenching to a temperature QT below M_S. The transformation rate parameter α_m is usually selected to be a constant value of 0.011 K^{-1} independent of composition. This value was derived by Koistinen and Marburger [44] through XRD analysis of Fe-C alloys at room temperature after quenching to temperatures as low as -79 °C. However, several researchers have suggested that the chemical composition does have an influence on the course of the martensitic transformation.[45] Therefore, in the present work, the rate parameter was instead calculated based on the local composition using the empirical equation proposed by Van Bohemen and Sietsma [45]:

$$\alpha_m(K^{-1}) = 0.0224 - 0.0107 w_C - 0.0007 w_{Mn} - 0.00005 w_{Ni} - 0.00012 w_{Cr} - 0.0001 w_{Mo} \tag{4.3}$$

where w_i is the amount of each alloying element in weight percent. This results in an α_m value of 0.0183 and 0.0167 for alloy MedC and MedCMn respectively. Figure 4.3 shows the resulting transformation curves for martensite as calculated using Equations 4.1, 4.2 and 4.3.

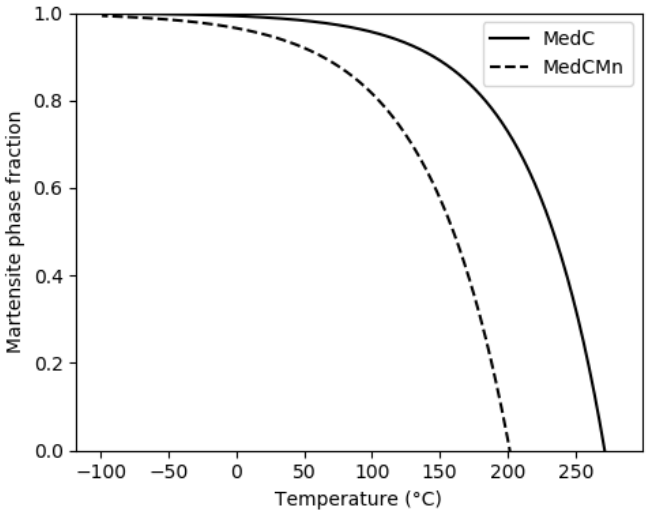

Figure 4.3: Volume fraction of martensite as a function of temperature calculated using Equations 4.1, 4.2 and 4.3.

According to the K-M model, quenching to room temperature (25 °C) results in a retained austenite phase fraction of 0.01 in alloy MedC and 0.05 in alloy MedCMn.

Besides the K-M model, the course of martensitic transformation was also investigated experimentally. By measuring the relative length change of a dilatometry specimen during quenching to room temperature, the relationship between temperature and martensite fraction can be estimated using the lever rule. Figure 4.4 shows an example of such a dilatometry trace for which the lever rule can be applied.

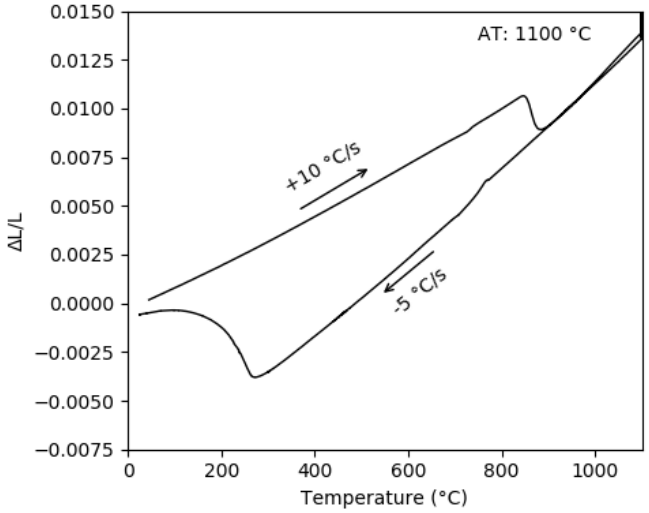

Figure 4.4: Relative length change of a MedC dilatometry specimen during heating to 1100 °C followed by continuous cooling at -5 °C/s to room temperature.

To convert the dilatometry data in martensite fraction versus temperature curves, several other parameters need to be known:

- The thermal expansion coefficient of austenite (CTE_{γ}).
- The thermal expansion coefficient of martensite ($CTE_{\alpha'}$).
- The volume fraction of martensite present at room temperature in the case of incomplete martensite transformation.

The thermal expansion coefficient of austenite can be determined fairly easily by fitting a linear regression line to the straight part of the cooling curve before the martensite transformation starts. Determination of the thermal expansion coefficient of martensite required an additional cooling and reheating step. After cooling at 5 °C/s to RT, specimens were held in liquid nitrogen for 20 minutes to form a fully martensitic structure. The specimens were then reheated in the dilatometer to 700 °C at 10 °C/s. The thermal expansion coefficient of martensite could then be determined by fitting a linear regression line to the straight reheating part of the change in length versus temperature curves.

According to XRD measurements, direct cooling to room temperature at 5 °C/s resulted in the retention of 0.01 austenite in the MedC specimen and approximately 0.02 in the MedCMn specimen. These values were considered in the lever rule calculation by vertically offsetting the coefficient of thermal expansion line of martensite accordingly.

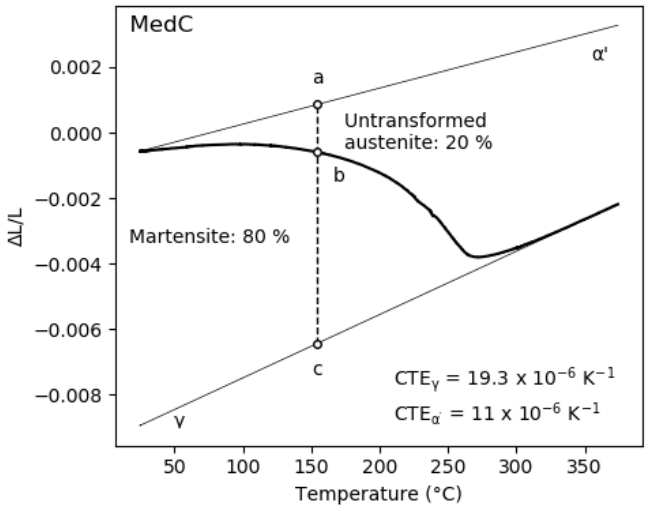

Figure 4.5: Thermal dilatation curve of a MedC dilatometry specimen around the martensitic transformation temperature showing the application of the lever rule (Equation 4.4).

Figure 4.5 shows how the martensite fraction at a specific quenching temperature can be determined with Equation 4.4. The thermal expansion coefficients of martensite and austenite used for the lever rule construction are also indicated.

$$\begin{aligned} f_{M_1} &= \frac{(b-c)}{(a-c)} \\ f_{\gamma} &= 1 - f_{M_1} \end{aligned} \tag{4.4}$$

The resulting martensite fraction versus temperature curves are presented in Figure 4.6.

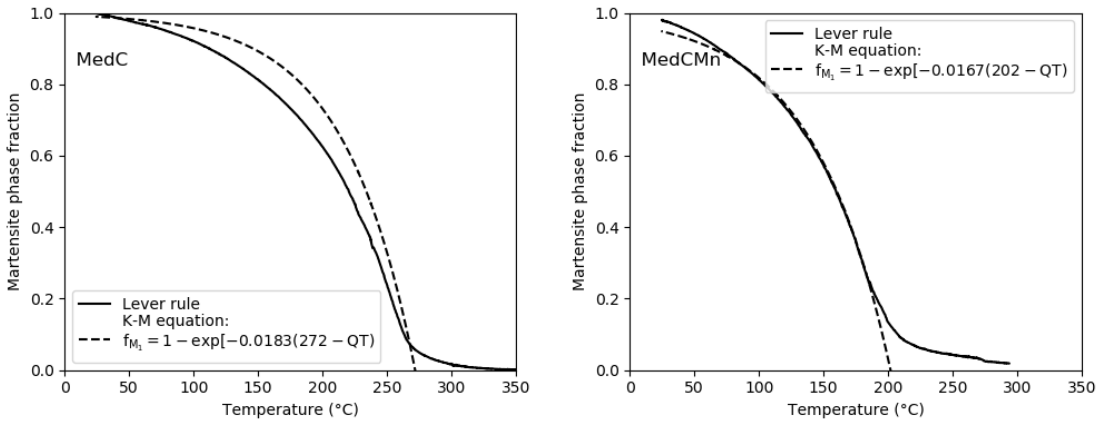

(a) (b)

Figure 4.6: Experimental volume fraction of martensite estimated from lever rule construction. (a) alloy MedC (b) alloy MedCMn. The dashed curves are calculated using Equations 4.1, 4.2 and 4.3.

The dashed lines represent the kinetics of alloy MedC and MedCMn calculated with Equations 4.1, 4.2 and 4.3. In Figure 4.6a it is seen that the difference with the experimental kinetics is quite large. Another drawback of the K-M equation is that it has a parabolic shape instead of a sigmoidal shape so it deviates significantly from experimental data for the initial 10-20 % of martensite formation. For alloy MedC, non-linear least-squares fitting of the K-M equation to the experimental data resulted in an α_m and $T_{K\text{-}M}$ value of 0.0148 and 267 °C, respectively (Figure 4.7). This α_m value is much lower than the one predicted using Equation 4.3 (0.0183).

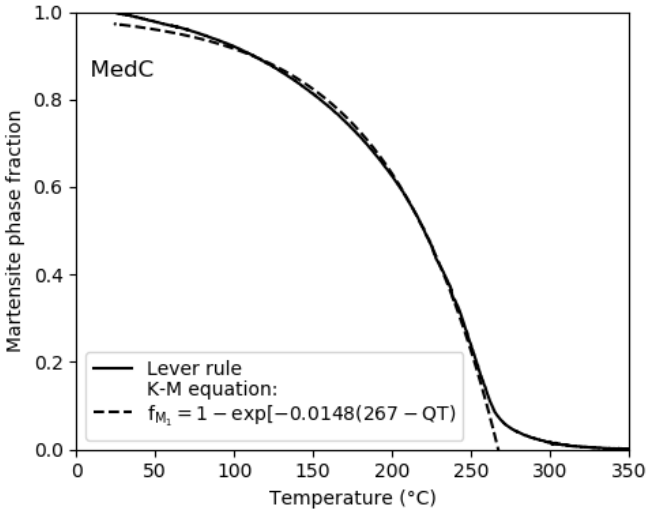

Figure 4.7: Non-linear least-squares fitting of the K-M equation to the experimental data.

These results demonstrate that the chemical composition does influence the progress of martensite formation, not only by its effect on the M_S temperature, but also the kinetics of martensite formation is composition dependent. From the experimental data, it is seen that the rate of transformation in alloy MedCMn is higher than in alloy MedC. However, the discrepancies between the calculated and measured values of α_m suggest

that Equation 4.3 is of limited use for the alloys used in this study. Van Bohemen and Sietsma also reported the largest discrepancies between calculated and measured values of α_m for steels that have high concentrations of Ni and Cr, and a relatively low carbon content.[45, 46]

4.2.4 Selection of quenching temperatures

To select quenching temperatures and estimate the retained austenite fraction for a given quenching temperature, a predictive model based on the Koistinen-Marburger equation as described by Speer et al. [12] was used. In this model, the volume fraction of primary martensite is first calculated using the K-M equation and Equations 4.1 and 4.3 for M_S and α_m. Because the material was fully austenitized prior to quenching, the untransformed austenite fraction at QT becomes:

$$f_\gamma = 1 - f_{M_1} \tag{4.5}$$

The model then assumes that all of the carbon in the primary martensite partitions into the untransformed austenite during the partitioning step (i.e. full partitioning assumption). With this assumption, the carbon content of the untransformed austenite after partitioning is:

$$w_C^\gamma = w_C^{alloy} / f_\gamma \tag{4.6}$$

where w_C^{alloy} is the carbon content in the bulk material. Equation 4.1 is then used once more to determine the M_S temperature of the carbon-enriched austenite (M_{S2}). Similarly, the rate parameter α_m is recalculated using Equation 4.3. Then, by applying the Koistinen-Marburger equation to the carbon-enriched untransformed austenite, the final phase fractions can be determined after final quenching to room temperature.

Following the steps as described above, the relationship between the quenching temperature and the retained austenite fraction (RA) in the final microstructure can be obtained. The model results for both alloys are shown in Figure 4.8. As can be seen in this figure, an optimal quenching temperature (OQT) exists where no fresh martensite forms during the final quench to room temperature, i.e. QT that leads to the maximum amount of retained austenite. For this OQT, the martensite start temperature of the carbon-enriched austenite (M_{S2}) is equal to RT. For alloy MedC, the maximum volume fraction of RA is estimated to be around 0.30 with a carbon content of 0.67 wt% and an OQT of 206 °C. For alloy MedCMn the maximum retained austenite fraction is 0.37 with a carbon content of 0.54 wt% and an OQT of 143 °C. Above the optimal quenching temperature, the austenite stability is too low during the final quenching step, and increasing amounts of fresh martensite start to form at higher quenching temperatures. Below the OQT, too much austenite is consumed during the initial quench to QT.

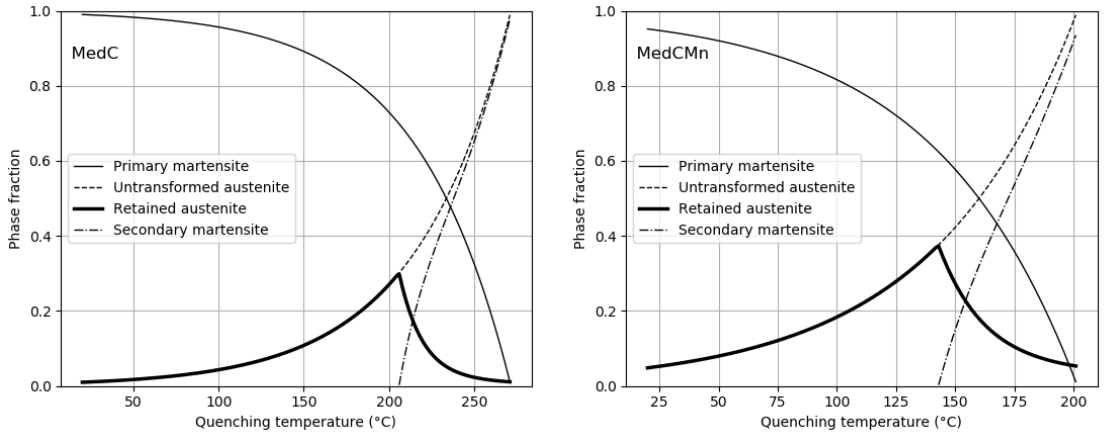

(a) (b)

Figure 4.8: Predicted Q&P microstructure evolution for (a) alloy MedC and (b) alloy MedCMn, assuming full carbon partitioning prior to final quenching to room temperature. The final volume fraction of retained austenite is given by the solid bold line.

As discussed in the previous section, the K-M model (with α_m from Equation 4.3) overestimates the rate of martensite formation for alloy MedC. Thus the OQT as predicted by the Speer model is likely too high. To get a more accurate prediction of the OQT, the experimental martensite kinetics as determined using the lever rule were used instead. This was done for both alloys so the two methods could be compared. Note that the fit of the K-M equation to the experimental data (Figure 4.7) could also be used in the Speer model to get a more accurate prediction of the OQT.

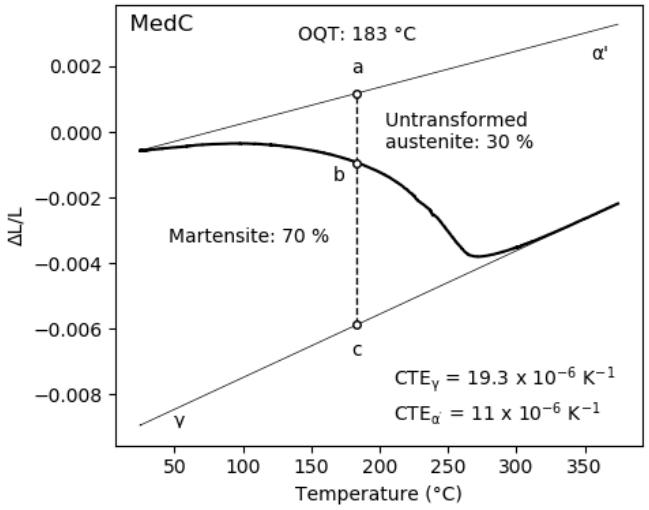

Figure 4.9: Optimal quenching temperature for alloy MedC as determined by applying the lever and Equation 4.1 for M_{S2} = RT.

As can be seen in Figure 4.9 the MedC OQT as determined using the lever rule is 183 °C. For alloy MedCMn, the OQT from lever rule calculation was determined to be 142 °C, which is in close agreement with the Speer model. A comparison between the OQT from the model and lever rule is given in Table 4.5.

Table 4.5: Comparison between OQT from model by Speer et al. and lever rule construction.

	MedC	**MedCMn**
C for M_{S2} = RT (Equation 4.1)	0.67 wt%	0.54 wt%
Max RA fraction (Equation 4.6)	0.30	0.37
OQT (model)	206 °C	143 °C
OQT (lever rule)	183 °C	142 °C

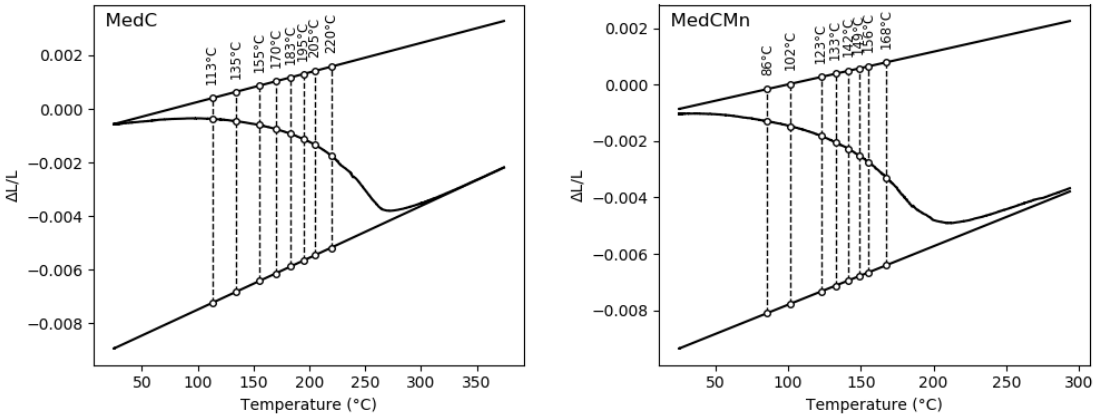

(a) (b)

Figure 4.10: Selected quenching temperatures for Q&P heat treatments for (a) alloy MedC and (b) alloy MedCMn.

To study the effect of quenching temperatures on the resulting microstructure, a range of quenching temperatures was selected around the OQT (Figure 4.10). All of the selected quenching temperatures and corresponding untransformed austenite fractions at QT are shown in Figure 4.11 and Table 4.6.

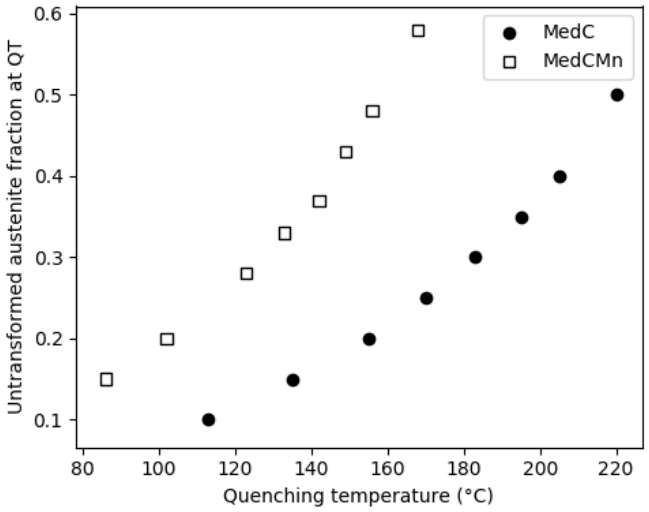

Figure 4.11: Selected quenching temperatures and corresponding untransformed austenite fraction at QT.

Table 4.6: Selected quenching temperatures for dilatometry experiments.

Sample ID	**QT (°C)**	**Untransformed austenite fraction at QT**
MedC A	113	0.10
MedC B	135	0.15
MedC 0	155	0.20
MedC C	170	0.25
MedC 2	**183**	**0.30**
MedC D	195	0.35
MedC 3	205	0.40
MedC E	220	0.50
MedCMn F	86	0.15
MedCMn G	102	0.20
MedCMn 4	123	0.28
MedCMn H	133	0.33
MedCMn 5	**142**	**0.37**
MedCMn i	149	0.43
MedCMn 6	156	0.48
MedCMn j	168	0.58

The fraction of primary martensite at QT is given by the microstructural balance:

$$f_\gamma + f_{M_1} = 1 \tag{4.7}$$

4.2.5 Holding time at the quenching temperature

The Q&P process often includes a short holding period at the quenching temperature to ensure that the material reaches a uniform temperature distribution. One of the QPINOX alloys with composition 0.30C-3.0Mn-0.35Si-13.0Cr was selected to investigate the possible effect of the holding time at the quenching temperature on the microstructural development. Dilatometry specimens were austenitized at 1100 °C for 15 minutes followed by cooling to 103 °C with a cooling rate of 5 °C/s. The specimens were held at this temperature for 5 s, 10 s, and 20 s. After this holding period, the heat treatment continued with a partitioning step at 400 °C for 2 minutes followed by quenching to room temperature.

An isothermal expansion could be observed at the quenching temperature indicating a temperature lag in the specimen, i.e. part of the austenite continues to transform into martensite when QT, as measured by the thermocouple, is reached. However, dilatometry curves corresponding to the different holding times showed identical martensite start temperatures of the carbon enriched austenite (M_{S2}). This indicates that a homogeneous temperature distribution is reached after less than 5 s at QT and no other microstructural changes take place during longer holding times at the quench temperature. Since there is no influence of the isothermal holding times evaluated, a holding period of 20 s was selected for the rest of the experiments.

4.2.6 Heating rate, partitioning conditions and final quench

For heating from quenching temperature to partitioning temperature, a heating rate of 10 °C/s was used. This fairly high heating rate ensures that most of the carbon partitioning takes place during the partitioning step and not during heating to the partitioning temperature. For the partitioning step, a fixed partitioning time and temperature of 5 minutes at 450 °C was selected, considering the literature on Q&P treatment of martensitic stainless steels [8, 5, 4]. As discussed in Section 2.2, it is expected that stable $M_{23}C_6$ carbides do not form at this temperature [4]. After the partitioning step, cooling to RT was performed at 5 °C/s, which is identical to the cooling rate used for the initial quench to QT.

4.3 Volume fraction of phases by dilatometry

Dilatometry specimens of both alloys were subjected to Q&P treatments with varying quenching temperatures as described in Section 4.2.4. The resulting strain versus temperature curves are shown in Figure 4.12.

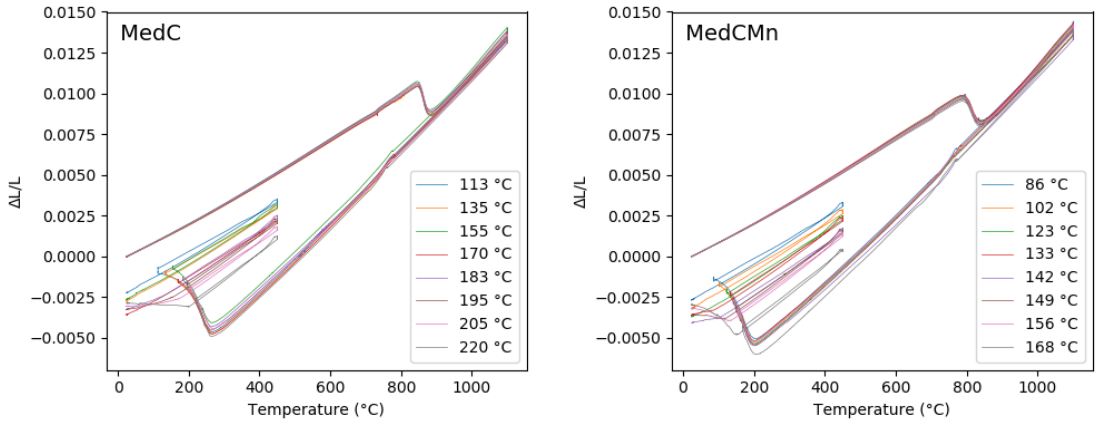

(a) (b)

Figure 4.12: Relative change in length of dilatometry specimens quenched from 1100 °C to different temperatures, reheated to 450 °C and soaked for 5 min, and quenched to room temperature for (a) alloy MedC and (b) alloy MedCMn.

The fraction of retained austenite in the Q&P processed dilatometry specimens was calculated by applying the lever rule at room temperature as described by Mola and De Cooman [4]. An example of this method is given in Figure 4.13. Point "d" indicates the strain in the absence of martensite formation and is obtained by extrapolating the austenite contraction curve. As mentioned in Section 4.2.3, XRD measurements indicated the presence of 0.02 retained austenite phase fraction after direct quenching to room temperature of alloy MedCMn. Therefore, in the lever rule calculations, it was assumed that the transformation strain "b" through "d" for uninterrupted quench only accounted for 98 percent of the strain expected in the absence of retained austenite.

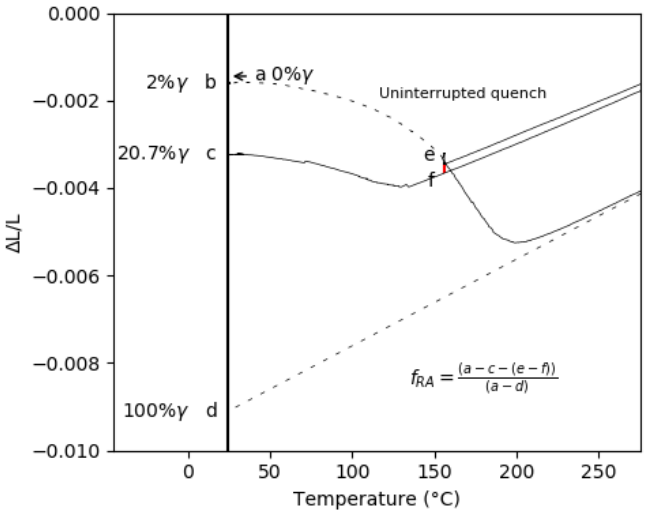

Figure 4.13: Demonstration of the lever rule application for the estimation of retained austenite fraction in the Q&P specimens.

As can be seen in Figures 4.12 and 4.13, the dilatometry curve during heating from QT to PT is not followed during the final quench to room temperature. Distance "e" through "f" (red line) indicates the irreversible strain which is associated with the tempering of primary martensite during the partitioning step [4]. Therefore, for the calculation of RA fraction, the irreversible strain is compensated for using the formula inserted in Figure 4.13.

The retained austenite phase fractions of Q&P processed specimens for different quenching temperatures are shown in Figure 4.14. For alloy MedC, the highest retained austenite fraction (0.22) was achieved at a quenching temperature of 183 °C. The optimal quenching temperature for alloy MedCMn was 142 °C, resulting in a retained austenite fraction of 0.295. The maximum fraction of retained austenite obtained in the dilatometry experiments did not reach the ideal amount predicted with CCE, which was 0.30 for alloy MedC and 0.37 for alloy MedCMn.

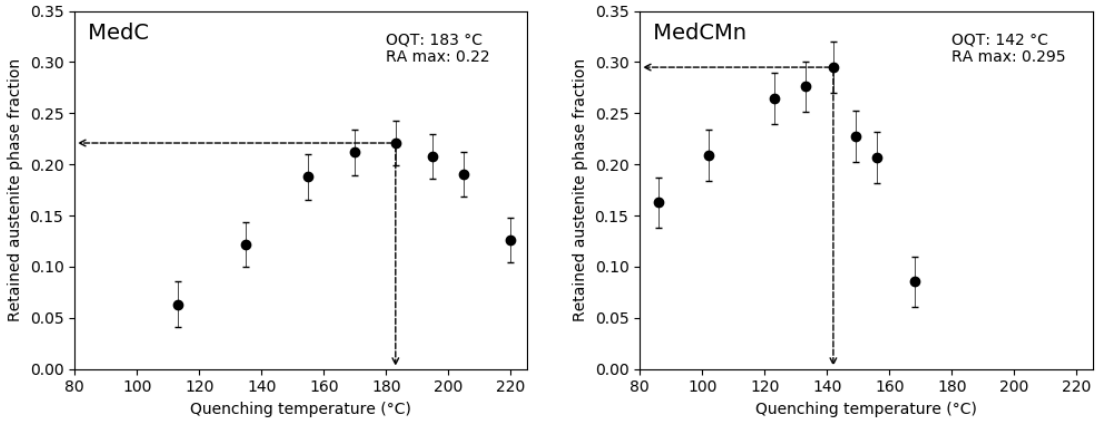

(a) (b)

Figure 4.14: Retained austenite phase fraction as a function of quenching temperature (a) alloy MedC and (b) alloy MedCMn.

The uncertainty (error bars) in the reported RA fractions mainly stems from measurement errors at the quench temperature. As can be seen in Figure 4.15, the strain versus temperature curves show an inexplicable jump in strain during the isothermal hold at the quenching temperature. Because these random jumps in strain have both positive values (e.g. for QT = 113 °C) as well as negative values (e.g. for QT = 183 °C), they are most likely related to the experimental setup. Besides this, there is another factor that results in an error in the calculated RA fractions. The fresh martensite that forms during the final quench forms from carbon enriched austenite, so the expansion associated with fresh martensite formation is not exactly the same as for primary martensite formation. The method as described by Mola and De Cooman to calculate the RA fraction does not take this into account. Using Equations 3.1, 3.2 and 3.3, it was estimated that this error is $<$ 0.5% in the samples with the highest fraction of M_2, so this is insignificant compared to the aforementioned measurement errors.

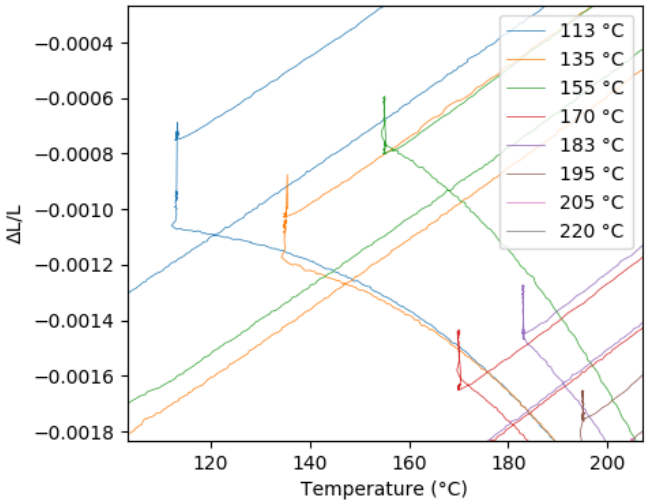

Figure 4.15: Inexplicable jumps in strain during the isothermal hold at the quenching temperature. Observed jumps were between two data points 0.1 seconds apart, i.e. not gradual over time.

Figure 4.16 summarises the different phase fractions that are present in each specimen. M_1 and RA were determined by applying the lever rule on dilatometry curves and M_2 was calculated using the microstructural balance. This means that errors in calculating M_1 and RA fractions lead to a cumulative error in f_{M_2}. The figure therefore wrongly suggests the presence of a small amount of M_2 in MedC specimens quenched to temperatures below 155 °C. Dilatometry curves of these specimens did not show any expansion associated with fresh martensite formation.

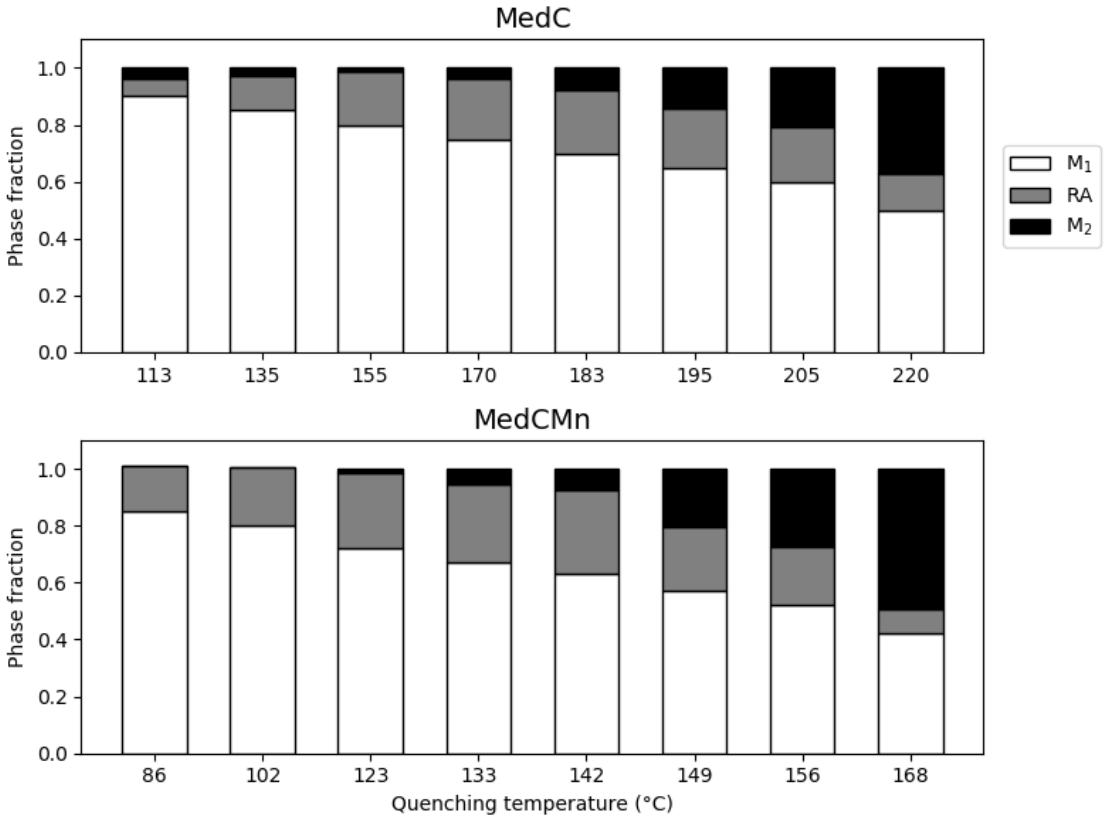

Figure 4.16: Phase fractions of Q&P processed specimens with different quenching temperatures. Primary martensite is denoted by M_1, retained austenite by RA and fresh martensite by M_2. M_1 and RA were determined by applying the lever rule on dilatometry curves and M_2 by the microstructural balance $f_{M_1} + f_{RA} + f_{M_2} = 1$.

4.4 Volume fraction of retained austenite by XRD

Besides dilatometry, the RA fractions in the Q&P processed specimens were also measured using XRD. The results of these experiments are shown in Figure 4.17. In specimens with severe preferred orientation or texture, it is reported that at least four austenite and ferrite diffraction peaks (n) are required to accurately determine the retained austenite fraction using Equations 3.4 and 3.5 [32, 47]. However, as described in Section 3.5, the {111} austenite peak overlapped with the {110} ferrite peak in the measured XRD patterns which led to an underestimation of the retained austenite fraction. Therefore, the RA fraction was also determined excluding the {111} an {110} peaks.

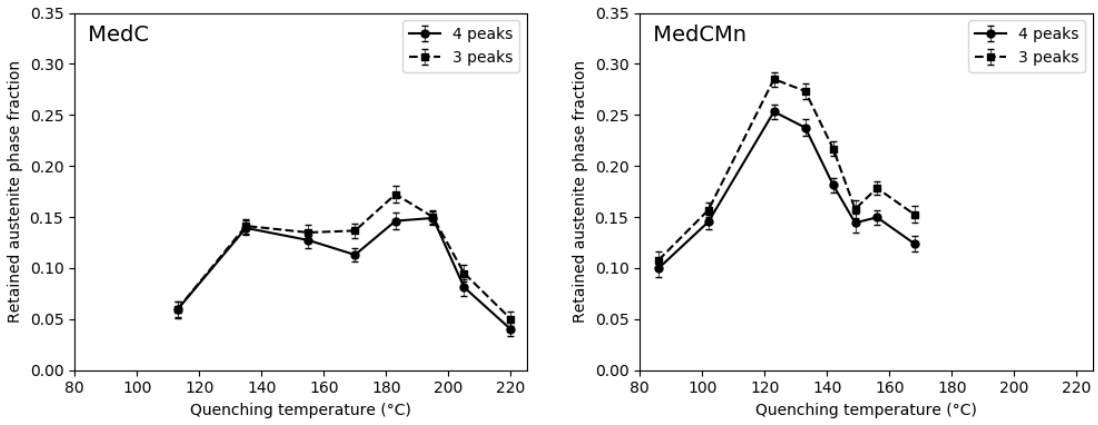

(a) (b)

Figure 4.17: Retained austenite phase fraction as a function of quenching temperature (a) alloy MedC and (b) alloy MedCMn. Phase fractions were measured using XRD as described in Section 3.5.

XRD measurements report much lower RA fractions than those determined by lever rule calculations. This difference might be attributed to the fact that polishing can cause mechanically-induced transformation of retained austenite. Another factor could be that a portion of the retained austenite on the specimen surface transformed to martensite after polishing due to the relief of constraints imposed by the surrounding grains. To study the effect of sample preparation on XRD measurements, the phase fractions of samples "MedC C 170C" and "MedCMn 5 142C" were remeasured after repolishing. Roughly 100 µm was removed from the scanned surface using wet grinding followed by polishing up to 0.04 µm OP-S diamond suspension with very light contact pressure.

The results of both the first and second XRD measurements are presented in Table 4.7. After repolishing, the RA fraction in sample "MedCMn 5 142C" as measured using XRD was actually 28% lower than before repolishing. Assuming that the RA distribution is homogeneous along the RD of the specimen, this indicates that sample preparation can have a significant effect on the amount of RA present at the scanning surface.

Table 4.7: Retained austenite fractions measured using XRD, before and after repolishing.

Sample ID	**Initial RA fraction**	**RA fraction after repolishing**
MedC C 170C	11.3 %	11.8 %
MedCMn 5 142C	18.1 %	13.0 %

4.5 Lattice parameter and carbon content of retained austenite

As discussed in Section 3.5, the change in austenite lattice parameter with quenching temperature was determined from the peak positions of the diffractograms. Figure 4.18 shows obtained diffractograms for Q&P processed specimens of alloy MedC with varying quenching temperatures. The austenite reflection peaks are at 2Theta angles of roughly 51, 60, 89, and 111 degrees.

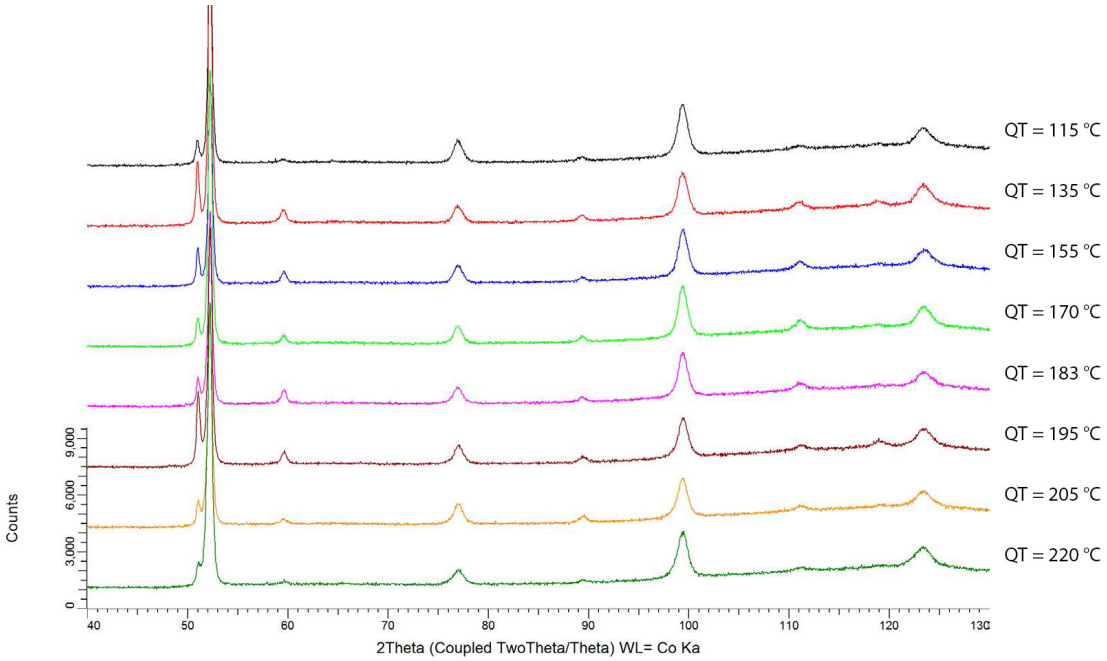

Figure 4.18: Diffractograms for MedC dilatometry specimens Q&P treated with different quenching temperatures and partitioning at 450 °C for 5 minutes.

The austenite lattice parameter as a function of austenite phase fraction at QT for alloys MedC and MedCMn is shown in Figure 4.19. In this case, the precise lattice parameter was determined as the average of the 4 diffraction peaks and the austenite phase fractions at QT were obtained from the data in Figure 4.6. The lattice expansion associated with carbon enrichment of the austenite increases at lower austenite phase fractions (i.e. lower quenching temperature).

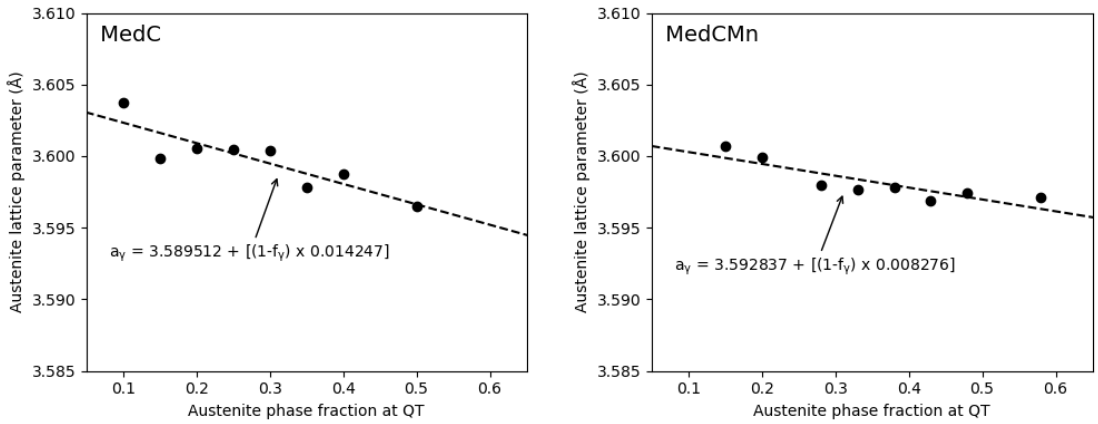

(a) (b)

Figure 4.19: Lattice parameter of Q&P processed specimens partition treated at 450 °C for 5 min as a function of austenite phase fraction at the quenching temperature for (a) alloy MedC and (b) alloy MedCMn.

When determining the lattice parameter using Cohen's method, no clear trend could be observed (see Figure 4.20). This might be attributed to the fact that when using Cohen's method to determine the precise lattice parameter, more weight is given to the

peaks corresponding to the highest θ values. This is done because the highest θ values are associated with smaller errors in the calculated lattice parameter (stemming from the $sin(\theta)$ term in the Bragg law). However, in the obtained XRD patterns, these reflection peaks were broad and small, making accurate determination of the peak positions difficult.

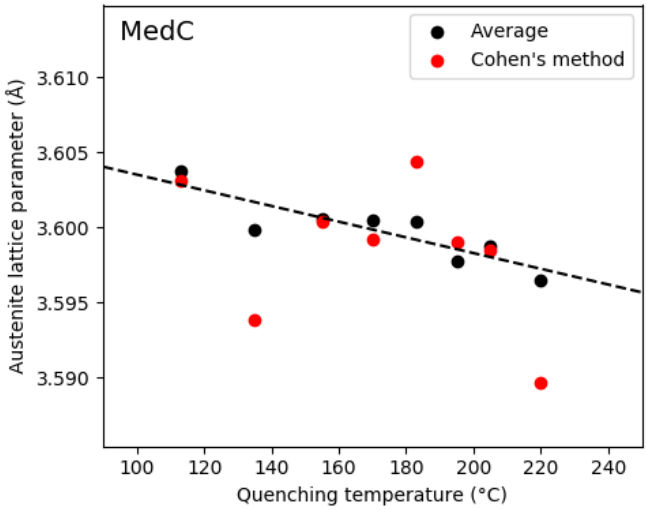

Figure 4.20: Precise austenite lattice parameter for alloy MedC determined from the average of 4 austenite reflection peaks and using Cohen's method (Section 3.5).

From the measured room temperature retained austenite lattice parameter, the retained austenite carbon content was estimated using existing empirical relationships (Equation 3.8 [35]). Figure 4.21 shows the change in carbon content with austenite phase fraction at QT. This figure also includes the theoretical maximum carbon content derived from the full partitioning assumption where all carbon is assumed to partition into the untransformed austenite.

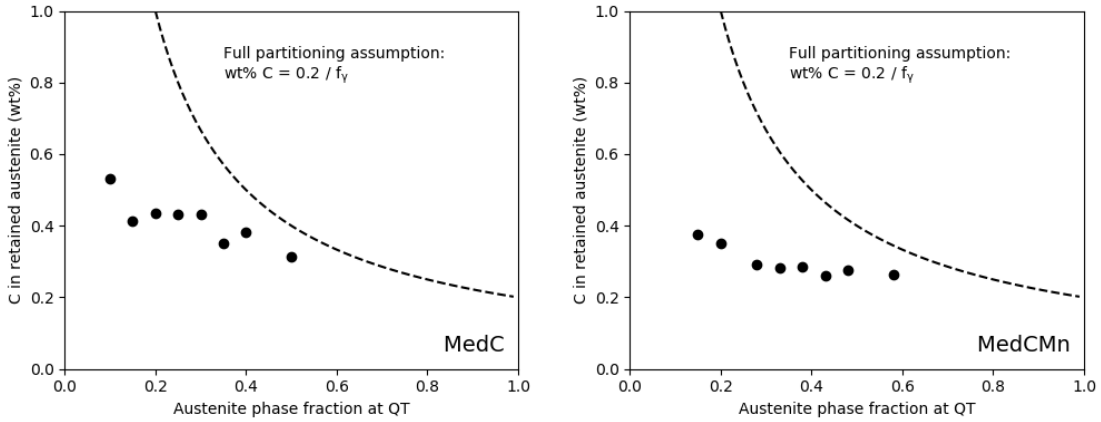

(a) (b)

Figure 4.21: Carbon content of austenite estimated from XRD measurements of austenite lattice parameter and Equation 3.8 [35] for (a) alloy MedC and (b) alloy MedCMn.

Note that the carbon content in the retained austenite is significantly lower than the full partitioning assumption, which suggests incomplete carbon partitioning or the occurrence

of other carbon consuming reactions such as carbide formation as will be discussed in Section 4.7.1.

4.6 Microstructures

The resulting microstructure after Q&P processing was studied using optical microscopy (OM), electron backscatter diffraction (EBSD) and electron probe micro analysis (EPMA).

4.6.1 Optical microscopy

Figure 4.22 shows optical micrographs of MedC and MedCMn specimens, quenched to 220 °C and 156 °C, respectively. Specimens were etched using Vilella's reagent, which is a popular etchant used for martensitic stainless steels. Nevertheless, it proved to be difficult to get consistent etching results with sufficient contrast between the different phases and grain boundaries. For this reason, only a limited number of optical micrographs are presented.

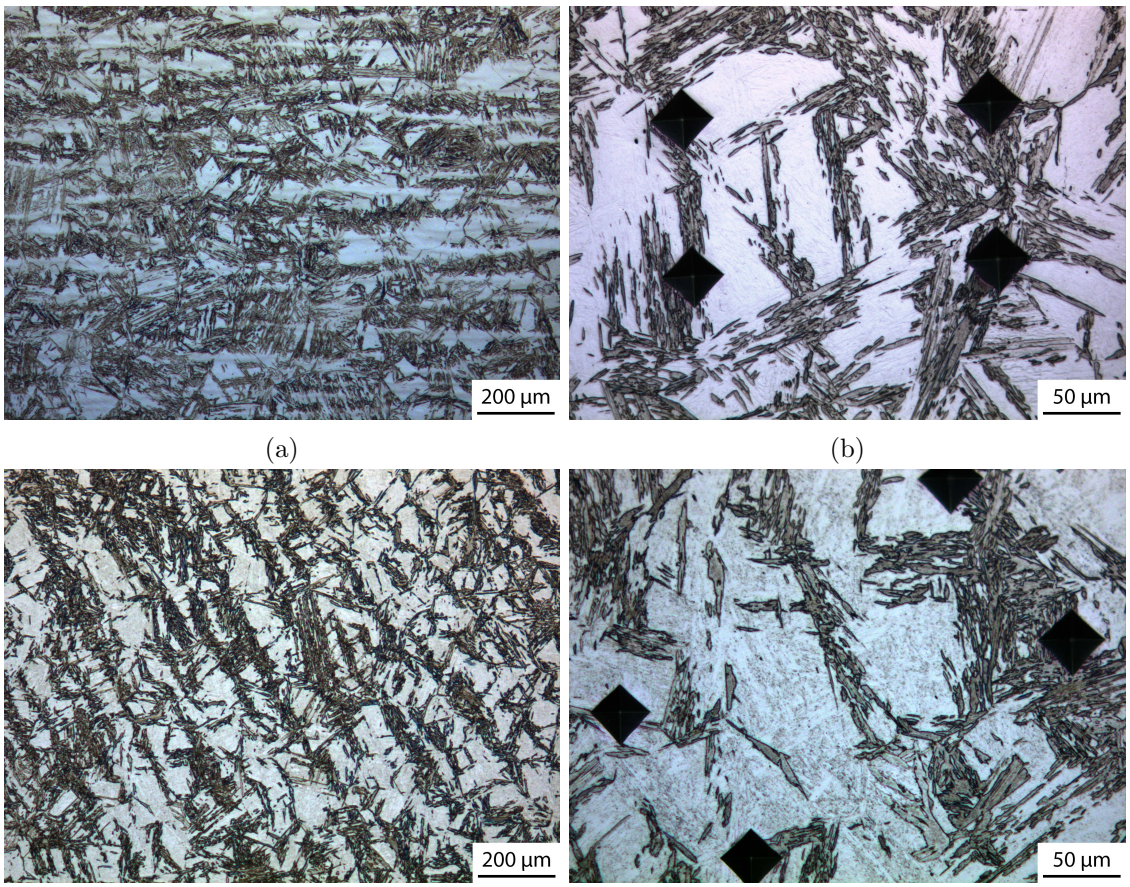

(a) (b)

(c) (d)

Figure 4.22: Optical micrographs of Q&P processed specimens partitioned at 450 °C for 5 minutes. (a) and (b) alloy MedC with QT 220 °C. (c) and (d) alloy MedCMn with QT 156 °C.

The primary martensite phase fraction is around 0.5 in both specimens. Although more pronounced in alloy MedCMn, both materials show significant microstructural banding parallel to the rolling direction. The darker, more etched regions indicate primary martensite that formed during the initial quench to QT and the lighter regions primarily consist of fresh martensite. It was difficult to determine if retained austenite existed in the microstructure or not from these pictures. Therefore, EBSD scans were performed in the areas marked by indents (Figure 4.22b and 4.22d) to identify the austenite and martensite phases.

4.6.2 Electron backscatter diffraction (EBSD)

Figure 4.23 shows EBSD orientation maps of Q&P processed MedC and MedCMn specimens revealing the presence of retained austenite. In Figure 4.23b, the different crystallographic orientations (colors) of the retained austenite indicate several prior austenite grains. In both specimens, the austenite fraction estimated from EBSD was much lower compared to XRD readings and dilatometry calculations. This might be attributed to the fact that a portion of the austenite transformed to martensite after polishing and/or some of the austenite grains have dimensions below the EBSD resolution. Furthermore, all EBSD scans required significant noise reduction due to the high number of zero solutions (EBSPs that could not be indexed). With a step size of 0.1 µm, the overall index rate was only around 40 %, which increased to 65 % with a step size of 0.05 µm. Therefore, EBSD mapping was only used to obtain qualitative data of retained austenite distribution.

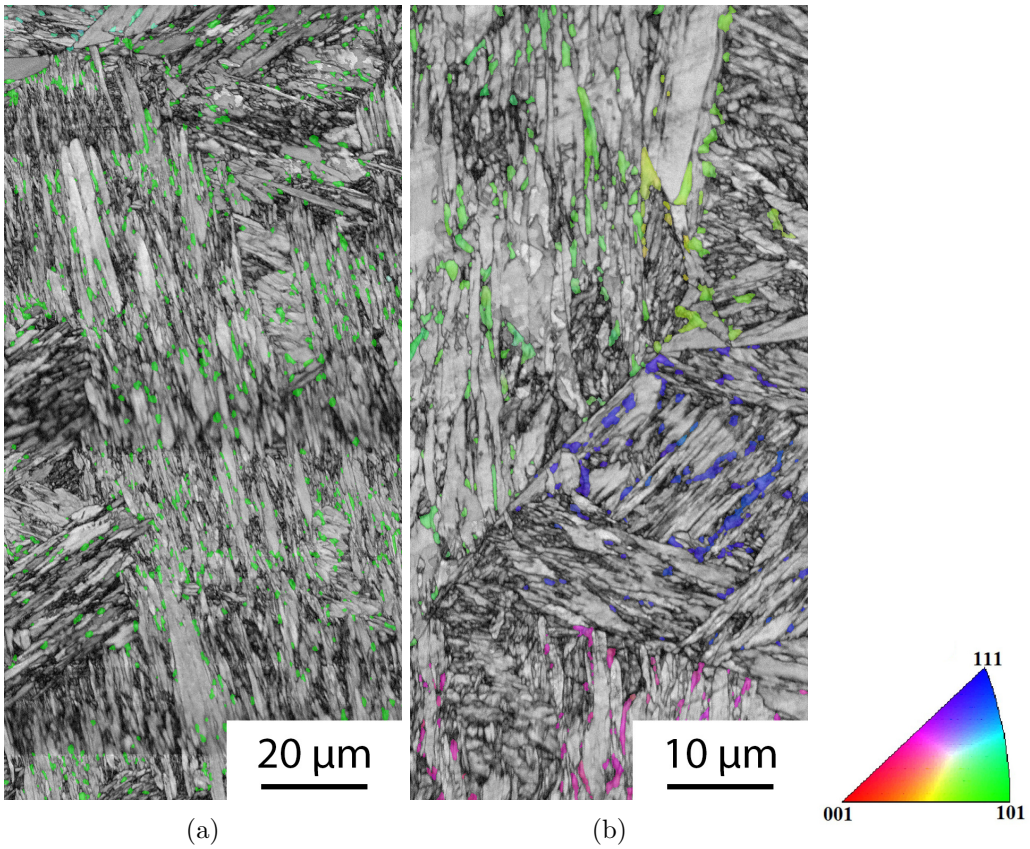

(a) (b)

Figure 4.23: Orientation imaging maps indicating crystal directions parallel to sheet normal direction (RD). Only the orientation of the austenite phase is shown. (a) MedC specimen with QT of 183 °C and step size of 0.1 µm. The retained austenite phase fraction observed in this figure is approximately 0.07. (b) MedCMn specimen with QT of 123 °C and step size of 0.05 µm. The retained austenite phase fraction observed in this figure is approximately 0.08.

Because primary martensite becomes carbon-depleted and tempered during the partitioning step, it can be assumed that the tetragonality of the martensite lattice will be different compared to the super-saturated fresh martensite that forms during the final quench to room temperature. However, the difference in tetragonility is generally insufficient for indexing of EBSPs. In this study, only the bcc and fcc phases were selected as matching units for indexing, so it was not possible to distinguish between tempered martensite (M_1) and fresh martensite (M_2) in the EBSD imaging maps, i.e. bcc represents M_1 + M_2. However, by comparing optical micrographs and EBSD phase maps of the same area, the location of retained austenite with respect to M_1 could be determined. Figures 4.24 and 4.25 show optical micrographs and EBSD phase maps of the same area for alloy MedC and MedCMn quenched to 220 °C and 156 °C, respectively.

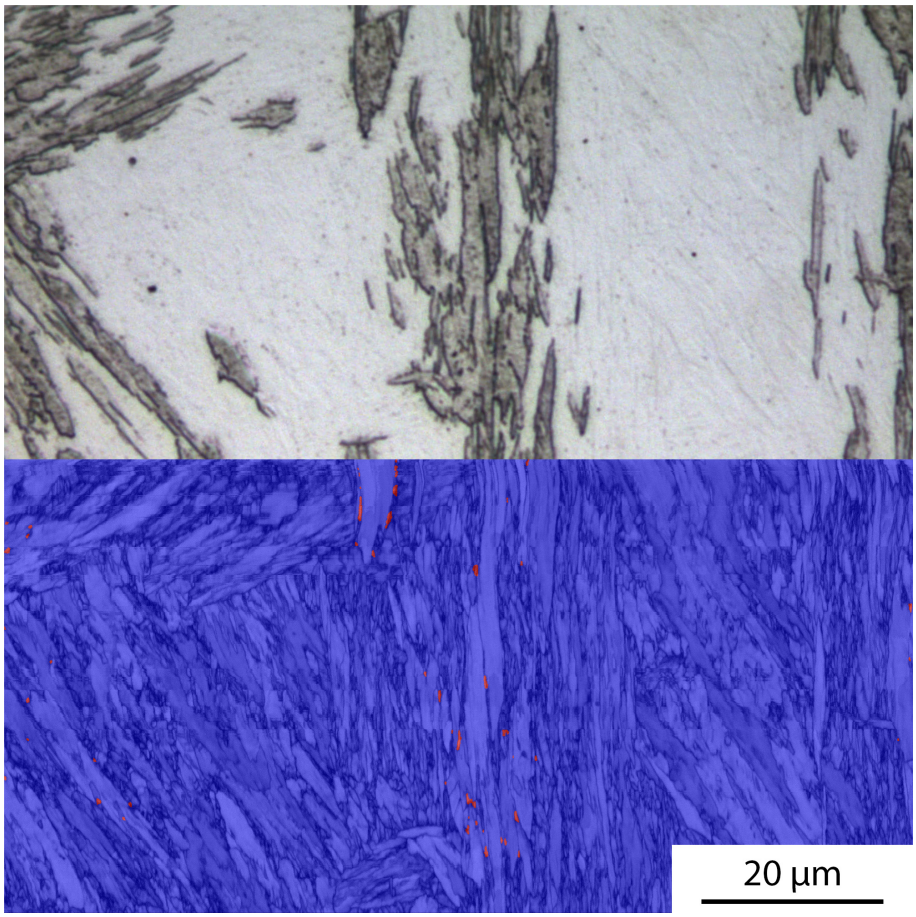

Figure 4.24: Optical micrograph and EBSD phase map of Q&P MedC specimen quenched to 220 °C and partitioned at 450 °C for 5 minutes. Red and blue indicate the austenite and martensite phase respectively. Scanning area is 2000x1000 pixels with a step size of 50 nm.

The blue areas in the EBSD phase map indicate primary and fresh martensite and the retained austenite grains are shown in red. By comparing the EBSD maps with the OM images, which show primary martensite as dark more etched regions, the location of the M_1 grains could be depicted in the EBSD maps. Of course, there is not a perfect match between the two images because a polishing step was required between etching for OM and EBSD surface preparation. Nevertheless, the individual M_1 grains can still be identified in both images.

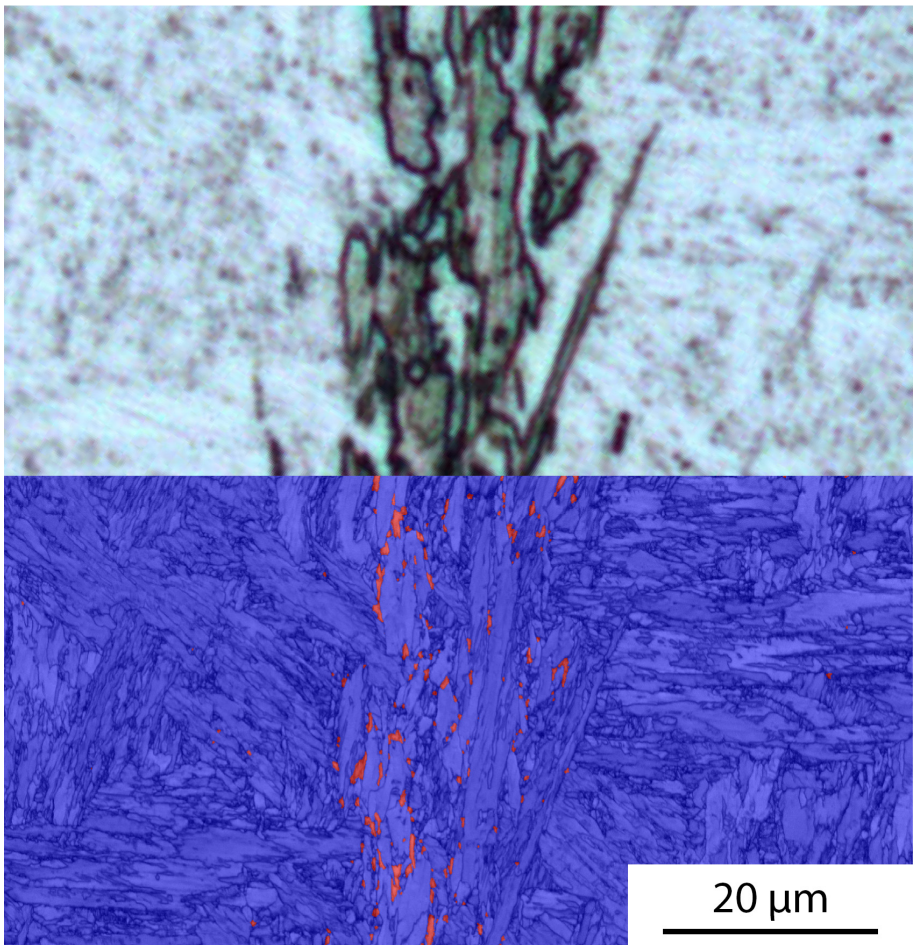

Figure 4.25: Optical micrograph and EBSD phase map of Q&P MedCMn specimen quenched to 156 °C and partitioned at 450 °C for 5 minutes. Red and blue indicate the austenite and martensite phase respectively. Scanning area is 1692x875 pixels with a step size of 50 nm.

The images revealed that retained austenite grains primarily existed on the primary martensite lath and A-M boundaries with an elongated shape along the boundaries and a size of $\sim$ 1 µm in width and up to several microns in length. This means that large regions of untransformed austenite did not get sufficiently enriched with carbon and transformed into fresh martensite upon the final quench to room temperature. Also, around thin regions of M_1, e.g. the needle like shape in Figure 4.25, hardly any austenite was retained. In other words, unlike the larger regions of M_1, these thin regions did not provide enough carbon for the stabilization of untransformed austenite.

To get a better understanding of the carbon enrichment process of the untransformed austenite, a phase field simulation of carbon partitioning was performed which will be discussed in more detail in Section 5.2.

4.7 Elemental distribution

As shown in the optical micrographs, the Q&P processed specimens show significant microstructural banding. Regions of M_1 and M_2 can be distinguished but is not clear to

what extent this banding is caused by alloying element segregation, and if so, by what element(s). To answer this question, electron probe micro analysis (EPMA) was performed on a Q&P processed specimen of alloy MedCMn. Figure 4.26 shows the analysis area locations for the two line scans and compositional mapping. Within this analysis area marked by indents, optical microscopy and EBSD had been performed prior to EPMA analysis.

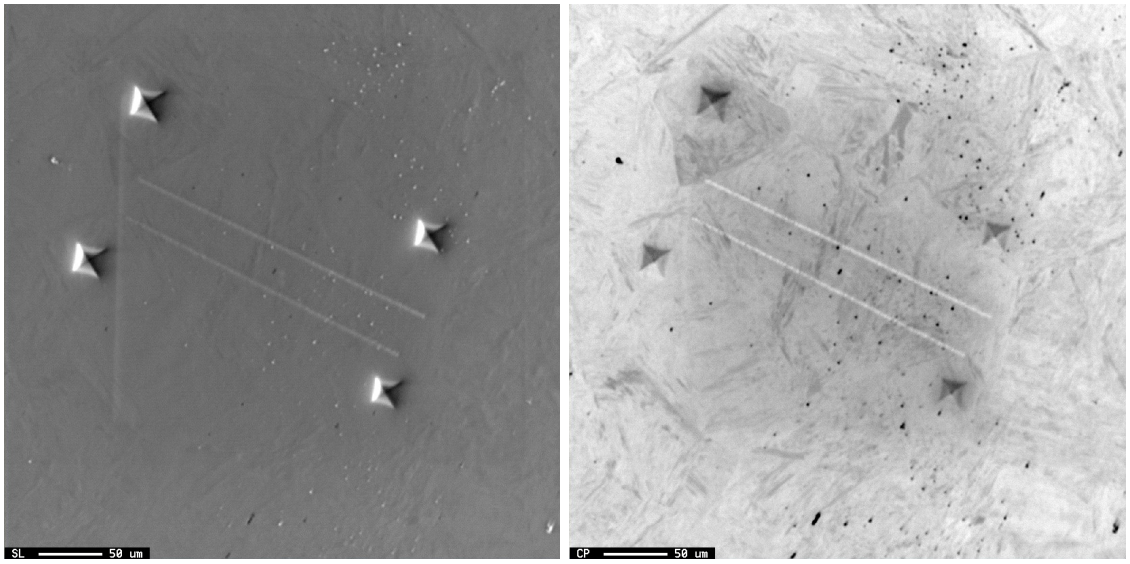

(a) (b)

Figure 4.26: The EPMA measurement locations on a Q&P processed MedCMn specimen with a QT of 156 °C are indicated by light bands marked in the (a) secondary electron image and (b) compositional backscatter electron image. Bottom line is identified as Line1 and top line as Line2.

The distribution of alloying elements Cr and Mn along Line1 (bottom line) is shown in Figure 4.27. The concentration of Cr and Mn varied between 11.9 and 13.2 wt% and 2.7 and 3.2 wt% respectively. It is seen that the variations in Mn and Cr concentration coincide with the microstructural bands. Furthermore, Mn follows the same trend as the variation in Cr concentration. The concentration of Si was also measured but no clear trend could be detected. Because the scatter in measurements was within the counting error for Si, the nominal Si concentration was assumed.

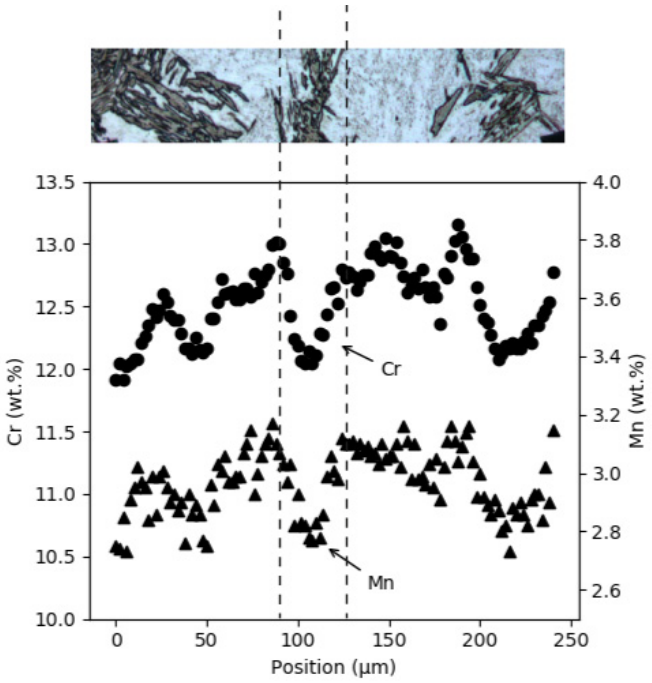

Figure 4.27: The distribution of Cr and Mn along Line1 (bottom line visible in Figure 4.26). The normal direction (ND) of the specimen is parallel to the horizontal axis.

Figure 4.27 clearly shows that in regions that primarily consist of M_1 (dark), the Cr and Mn concentration is lower than in regions with mostly M_2 (light). Because the M_S temperature increases with decreasing Mn and Cr concentration (Equation 4.1), primary martensite starts to form earlier in the Cr/Mn-poor regions during the initial quench to QT than in the Cr/Mn-rich regions.

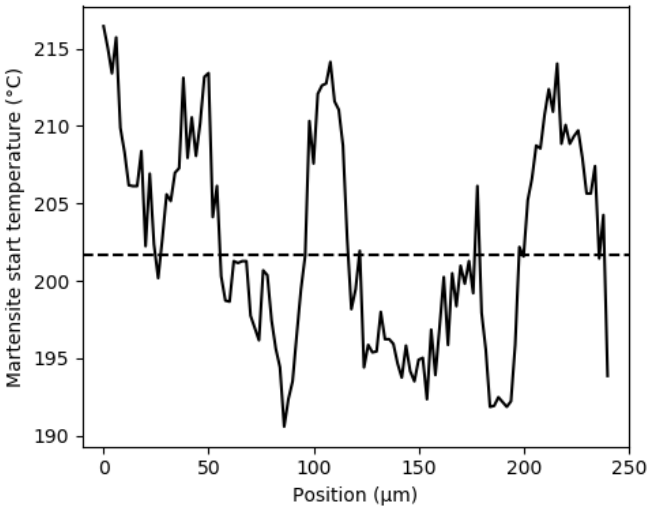

Figure 4.28: Variation in martensite start temperature along Line1. Dashed line indicates the M_S temperature for the base composition (Table 3.1).

This can be seen in Figure 4.28, which shows the variation in martensite start temperature along Line1. M_S was calculated using Equation 4.1, only considering the measured

variation in Mn and Cr. For the other alloying elements the base composition was assumed. It is seen that the M_S temperature varies approximately 25 °C between Mn/Cr-poor regions and Mn/Cr-rich regions. However, in reality, the variation in M_S is likely even greater, due to the expected segregation of C at the austenitization temperature. Mn lowers the chemical potential of carbon in austenite, which causes carbon to diffuse from Mn-poor regions to Mn-rich regions.[22] Hence, a non-uniform C distribution along the ND after austenitization can also be expected. In Mn-poor and Mn-rich regions, the C concentration is expected to be respectively lower and higher than the base composition after austenitization which leads to an even greater variation in M_S temperature during the initial quench than is shown in Figure 4.28. To measure the extent of carbon segregation after austenitization, quantitative EPMA analysis could be performed on an austenitized and fully quenched specimen. Another method for determining the segregation of carbon could be to calculate the equilibrium carbon concentration at the austenitizing temperature in relation to the Mn and Cr concentration, e.g. using ThermoCalc.

Quantitative EPMA analysis (line scans) of the carbon distribution of a Q&P processed specimen was also attempted but failed due to difficulties in the decontamination procedure. Qualitative mapping of the C distribution (Figure 4.29) did not show any significant variation in C content (banding) after Q&P treatment.

4.7.1 Presence of carbides and silicides

Besides the quantitative EPMA analysis, qualitative composition mapping was also performed. In the figures below, compositional maps of C, Mn, Si, and Cr are presented.

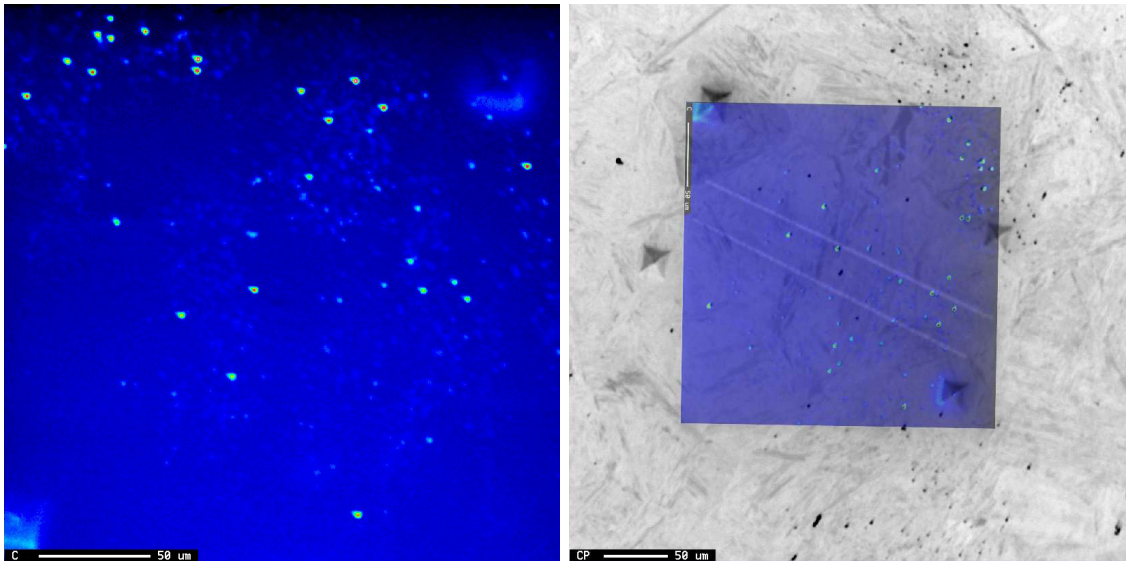

(a) (b)

Figure 4.29: (a) Compositional map of carbon (b) overlaid onto backscattered electron image showing the presence of carbides.

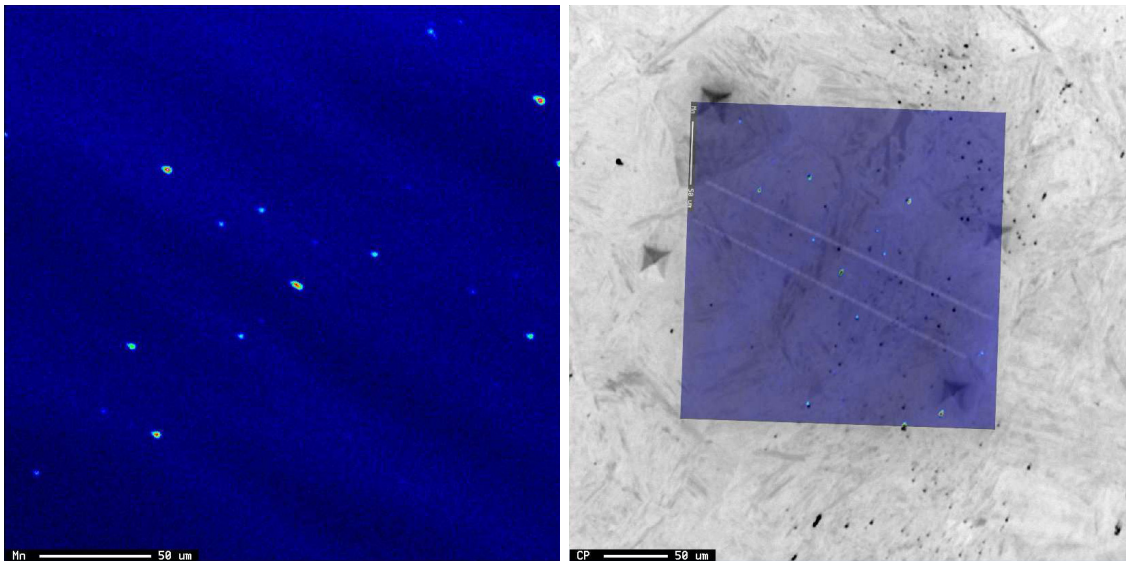

(a) (b)

Figure 4.30: (a) Compositional map of manganese. (b) overlaid onto backscattered electron image.

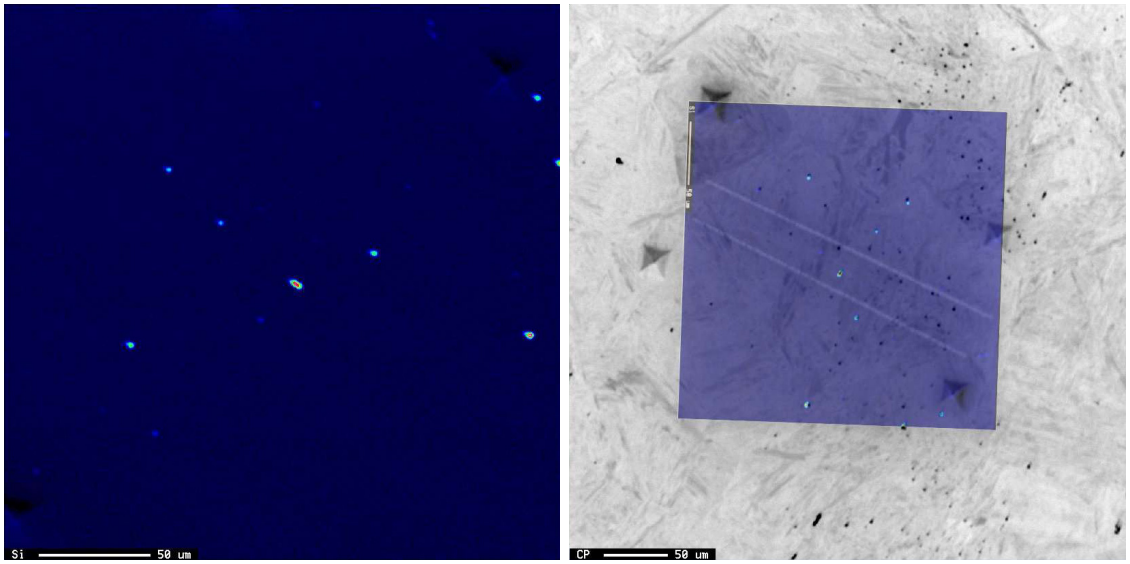

(a) (b)

Figure 4.31: (a) Compositional map of silicon. (b) overlaid onto backscattered electron image.

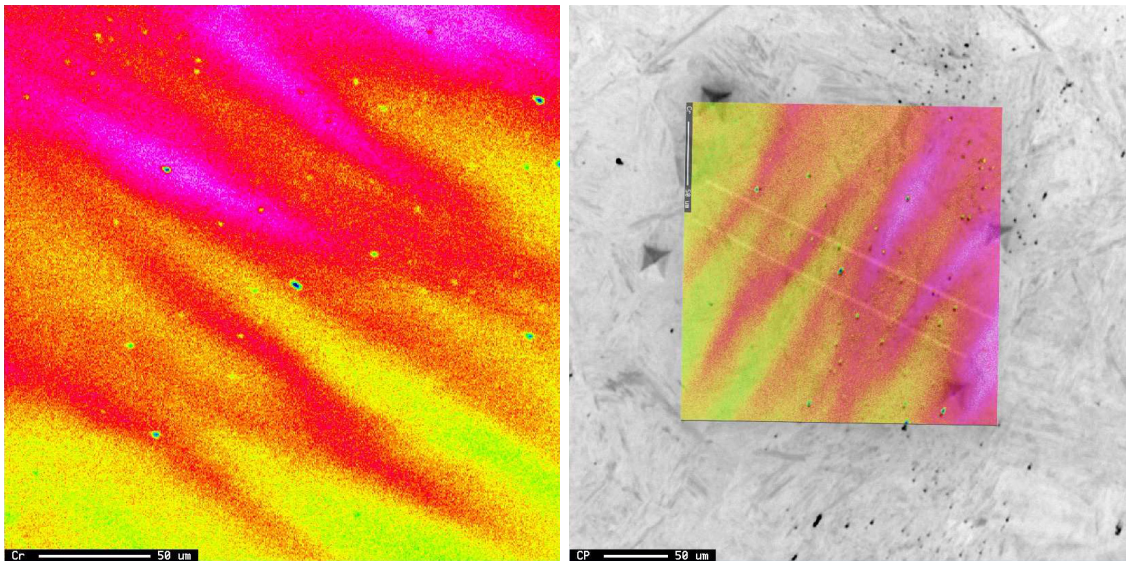

(a) (b)

Figure 4.32: (a) Compositional map of chromium. (b) overlaid onto backscattered electron image.

In Figures 4.30 and 4.33, the segregation of Mn and Cr into bands is clearly visible. Note that the Cr map is slightly disturbed by the instability of the beam current. The Si and C maps do not show significant elemental segregation.

The compositional maps reveal the presence of precipitates with element concentrations that are different from their surroundings. By overlaying the different compositional maps onto each other, two types of precipitates can be identified. Figure 4.33a shows precipitates containing elevated levels of carbon and a chromium concentration below the base composition (circled in white). These precipitates are most likely cementite as stable Cr-rich carbides such as $M_{23}C_6$ only start to form at temperatures above 480 °C.[4] Figure 4.33b shows that silicides containing manganese and chromium are also present. The exact composition of the precipitates could not be determined from these maps.

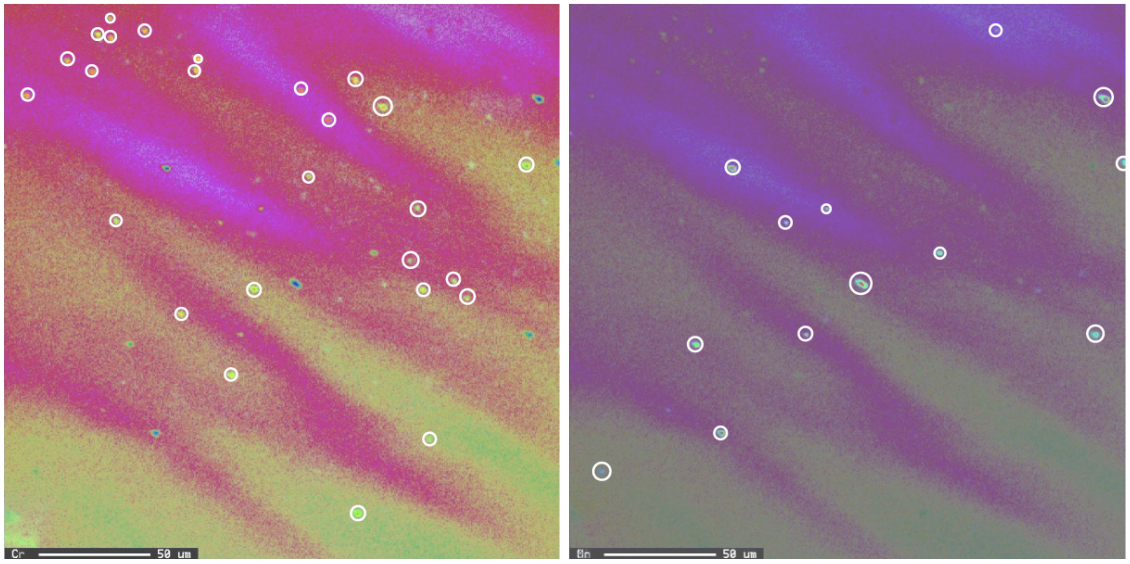

(a) (b)

Figure 4.33: Compositional maps overlaid on top of each other showing two types of precipitates circled in white. (a) Carbides (b) Silicides containing manganese and chromium.

Chapter 5

Discussion

5.1 Assessment of phase fractions and carbon in phases

As explained in Sections 4.3 and 4.4, the volume fraction of retained austenite after Q&P treatment was determined in two ways: dilatometry and XRD. Figure 5.1 shows a comparison of the two methods. It is seen that there is a large discrepancy between the two measurements and that, in general, XRD reports much lower RA fractions than dilatometry calculations. Similar differences have been reported by Mola and De Cooman [4].

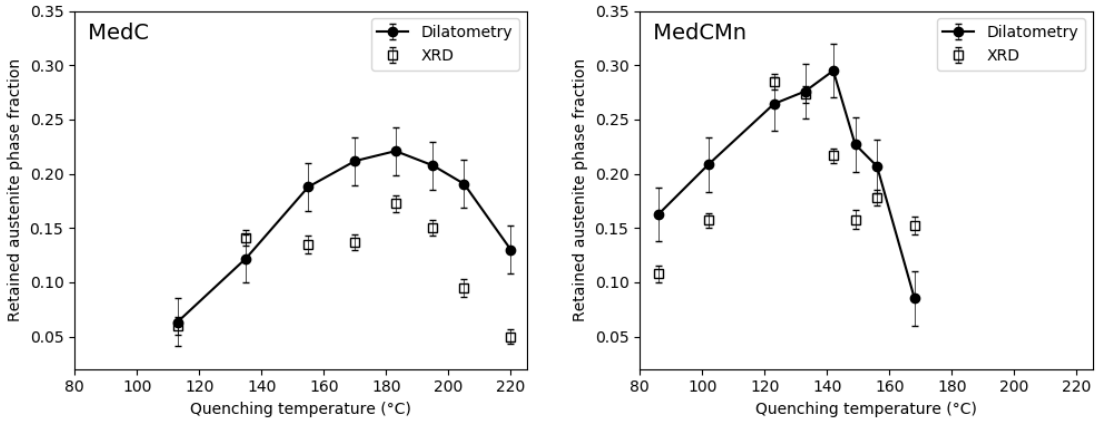

(a) (b)

Figure 5.1: Retained austenite phase fraction as a function of quenching temperature. Phase fractions are determined as described in Sections 4.3 and 4.4. XRD phase fraction correspond to 3 reflection peaks. (a) alloy MedC and (b) alloy MedCMn.

This difference can most likely be attributed to the fact that some of the retained austenite on the specimen surface transformed to martensite after polishing due to the relief of constraints imposed by the surrounding grains or mechanically-induced transformation (see Table 4.7). Other aspects that negatively influence the accuracy of the XRD measurements are the overlapping peaks and the small specimen size (low number of crystallites that contribute to the measured pattern). In this study, dilatometry lever rule calculations are thought to give a more accurate measurement of the RA present in the heat-treated samples, but other methods such as saturation magnetization should be

considered as well.

Based on the dilatometry results, the maximum RA fractions in alloys MedC and MedCMn are approximately 0.22 and 0.3, respectively. The corresponding optimal quenching temperatures (183 °C and 142 °C) were correctly predicted by applying the lever rule and Equation 4.1 for M_{S2}= RT. It is clear that Mn addition lowers the optimal quenching temperature and increases the maximum retained austenite fraction that can be obtained by applying a Q&P treatment to martensitic stainless steels. In alloy MedC and MedCMn, the measured retained austenite fraction reached 75% and 79% of the ideal amount predicted with CCE and the full partitioning assumption.

As can be seen in Figure 5.2, both alloys show a similar trend between primary martensite fraction and retained austenite fraction. However, for the same primary martensite/untransformed austenite fraction at QT, a higher fraction of austenite is retained after the partitioning step for the high-Mn alloy. From these figures, it is not directly clear whether this increase in retained austenite fraction is solely caused by the stabilization effect of manganese, or if (also) more carbon partitioned into the untransformed austenite in the high-Mn specimens compared to the low-Mn specimens.

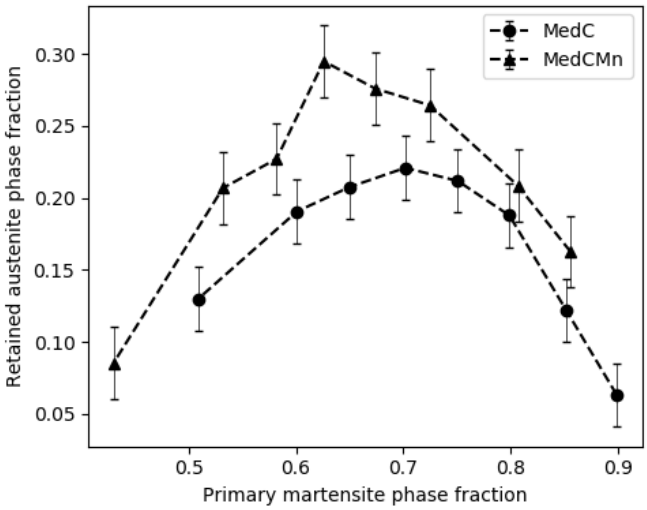

Figure 5.2: Retained austenite fraction versus primary martensite fraction.

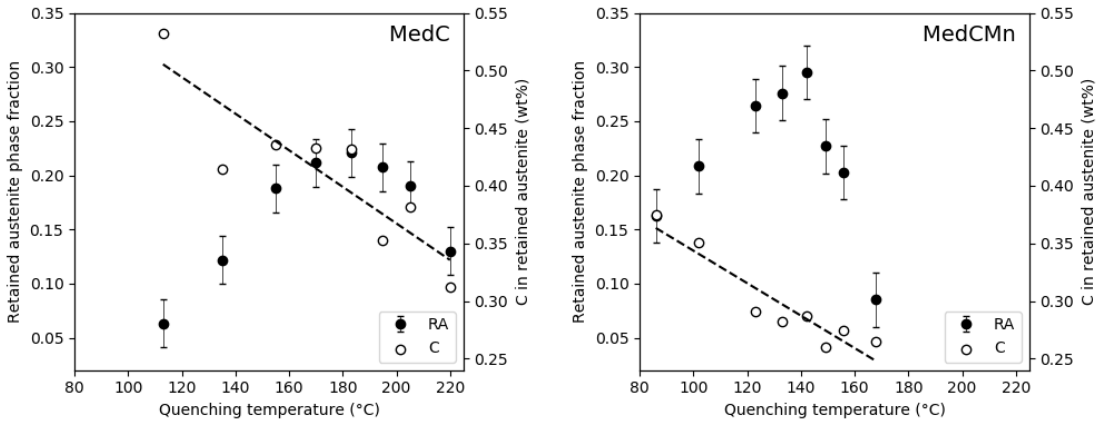

(a) (b)

Figure 5.3: Retained austenite phase fraction and carbon content as a function of quenching temperature (a) alloy MedC and (b) alloy MedCMn.

Figure 5.3 shows that, as expected, the carbon concentration of the retained austenite increases with decreasing quenching temperature. The rate of increase is nearly identical between the two alloys. However, as is shown in Figure 5.4, the carbon concentration in the retained austenite is higher in alloy MedC than in alloy MedCMn. Nevertheless, a higher volume fraction of retained austenite was stabilized in alloy MedCMn for the same phase fraction of untransformed austenite/primary martensite at QT (Figure 5.2).

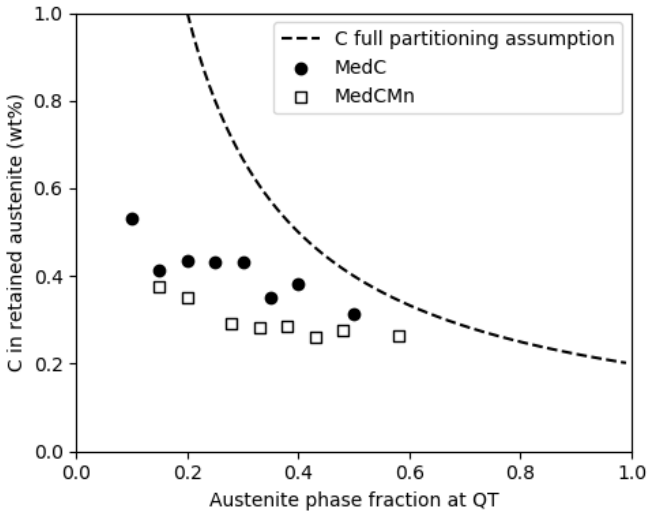

Figure 5.4: Comparison of carbon concentration in austenite between alloy MedC and MedCMn.

This can be explained by the difference in critical carbon concentration between the two alloys (i.e. w_C for which $M_{S2} \leq RT$). In alloy MedC, the critical carbon concentration is 0.132 wt% higher than in alloy MedCMn due to difference in Mn concentration (Equation 4.1). Thus, more carbon would need to partition into the untransformed austenite during the partitioning step in order to stabilize the same amount of retained austenite in both alloys. Regardless of Mn concentration, the carbon enrichment of austenite was well below the enrichment expected based on the full partitioning assumption. In other words,

not all of the carbon in the supersaturated martensite partitioned into the untransformed austenite during the partitioning step. This is in line with the experimental observation of the carbon concentration of austenite in Q&P processed martensitic stainless steels remaining well below the value calculated based on the full partitioning assumption. [4, 5, 6, 7, 17] Carbide formation, as was shown in Figure 4.33a, was one of the mechanisms competing with the carbon enrichment of austenite. Despite this, large fractions of austenite were stabilized to room temperature which suggests the occurrence of other non-chemical stabilization mechanisms. Long and short range diffusion of carbon to potential martensite nucleation sites (A-M boundaries and austenite lattice micro strains) as well as grain refinement and hydrostatic stresses are some other recognized mechanisms that also contribute to the austenite stability. [4, 17, 48]

Huang et al. [17] have also shown that the extent of carbon partitioning is not simply proportional to the primary martensite fraction [2] but also depends on the size and distribution of martensite plates. In Q&P processing, the carbon in supersaturated martensite can segregate to the A-M phase boundaries already at the quench temperature. During partitioning, the segregated carbon at the A-M boundaries supplies the carbon that is needed for the stabilization of untransformed austenite.[20] Hence, the A-M boundary area or size and distribution of primary martensite plates also influences the carbon enrichment of the untransformed austenite. Optical micrographs did not show a significant difference in primary martensite morphology/A-M boundary area between the two alloys for the same fraction of primary martensite at QT. Thus in this study, the higher retained austenite fractions observed in the high-Mn alloy are not thought to be caused by a difference in martensite morphology/A-M boundary area between the two alloys.

5.2 Phase field simulation (PFM) of carbon partitioning

To get a better understanding of the partitioning process and the influence of microstructure morphology on the carbon enrichment of untransformed austenite, a phase field simulation of carbon partitioning was performed.

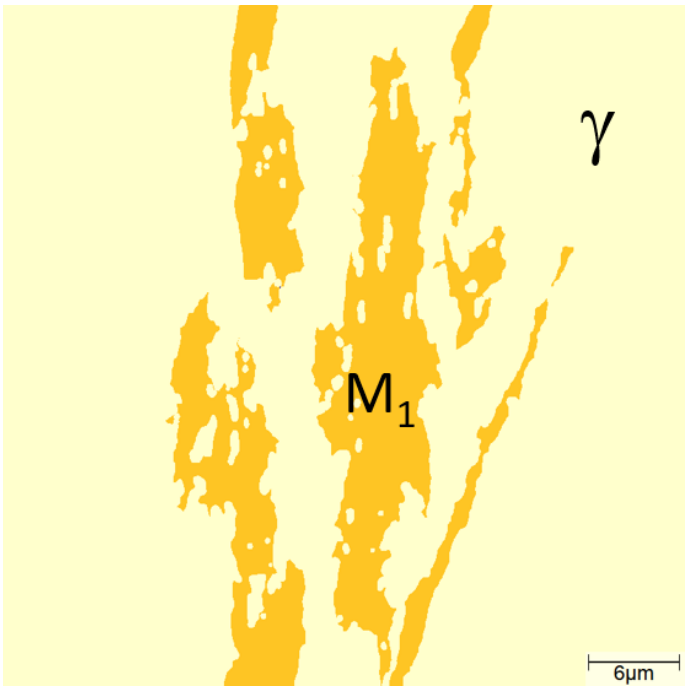

Figure 5.5: Initial microstructure for phase field simulation.

The combination of optical microscopy and EBSD that is presented in this study, gives insight in the microstructure that is present midway through the Q&P treatment at the onset of partitioning. At this point, the microstructure consists of primary martensite and untransformed austenite.

Using Channel 5 Tango software and the OM image as a reference, the M_1 grains could be depicted in the EBSD image of a Q&P treated MedCMn specimen quenched to 156 °C (Figure 4.25). This microstructure consisting of M_1 and untransformed austenite was used as the input for a phase field simulation of carbon partitioning from martensite into austenite (Figure 5.5). This simulation was performed by Dr. M.G. Mecozzi at TU Delft using MICRESS and Thermo-Calc software. Phase field simulations of the Q&P treatment have been performed before [49], but it is generally difficult to obtain an accurate initial microstructure. A common practice is to first simulate the formation of primary martensite during the initial quench to obtain an input microstructure for the simulation of the partitioning process. In this study, this microstructure was obtained experimentally instead. For the simulation, a homogeneous distribution of the alloying elements was assumed at the beginning of the partitioning step as presented in Table 3.1. Figure 5.6 shows the carbon distribution in wt% after partitioning at 450 °C for 300 seconds.

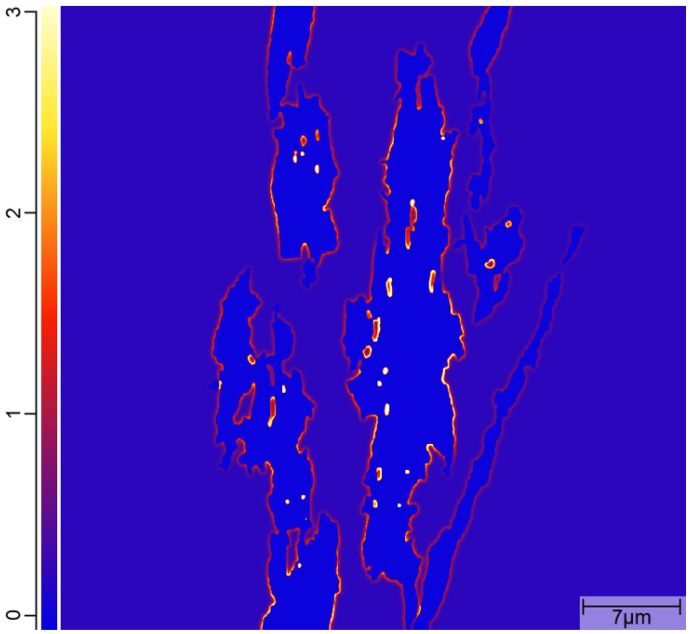

Figure 5.6: Carbon distribution in wt% after partitioning at 450 °C for 5 minutes.

It can be seen that the M_1 grains become depleted of carbon and that most of the carbon accumulates at the A-M boundaries. After the partitioning step, all untransformed austenite that is not sufficiently enriched with carbon will transform into fresh martensite (M_2) upon the final quench to room temperature. Using Equation 4.1 with M_S set to RT, it was calculated that for alloy MedCMn, the minimum carbon concentration for stabilization of austenite is 0.54 wt%. Figure 5.7a shows the result of the phase field simulation, indicating the retained austenite with a carbon concentration of 0.54 wt% or higher.

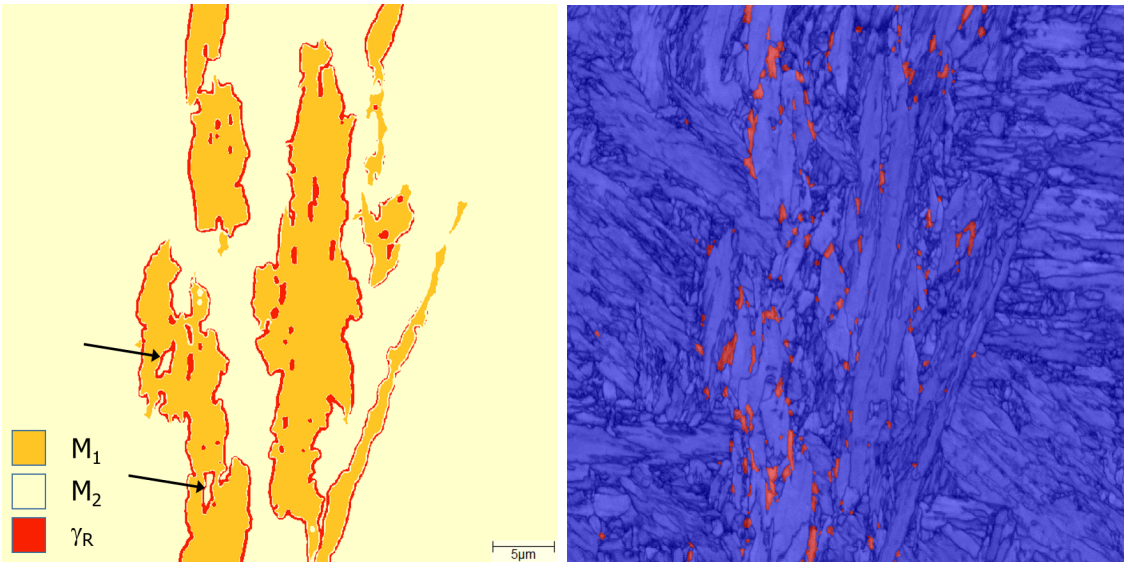

(a) (b)

Figure 5.7: (a) Phase field model simulation result, showing retained austenite with a carbon concentration of >0.54 wt% in red. (b) EBSD phase map showing martensite in blue and retained austenite in red.

The 2D phase field simulation shows a thin film of retained austenite around the M_1 grains and larger areas of RA completely surrounded by M_1. The EBSD map of the final microstructure (Figure 5.7b) shows retained austenite grains of a similar size, which suggests that the model fairly accurately predicts the carbon partitioning process. A difference between the simulation and the EBSD map is that no continuous film of RA is observed in the EBSD map. This could be related to the fact that the model is only a 2D simulation and does not include the formation of carbon-consuming carbides during partitioning. Also, the diffusion of carbon to martensite defects and segregation of alloying elements is not included in the simulation. In addition, some of the retained austenite was likely lost or incorrectly indexed in the EBSD map due to the low index rate and the noise reduction procedure that was used.

One interesting observation is that the center of the islands of untransformed austenite with a size of approximately 2 x 4 µm (marked by arrows in Figure 5.7a) transformed into fresh martensite in the simulation but not in the EBSD phase map. This could mean that other stabilization mechanisms such as hydrostatic stresses imposed by the surrounding primary martensite grains lead to the stabilization of austenite with a carbon content below the critical carbon concentration.

Both EBSD scans and phase field simulations showed that the retained austenite grains have a limited size of only $\sim$ 1 µm in width and up to several microns in length. The small size of the retained austenite grains can be explained by the maximum diffusion distance of carbon in austenite during the partitioning step. For a binary Fe-C austenite, the lattice diffusion distance of carbon can be estimated as $2.4\sqrt{(Dt)}$ [50] with D in m^2s^{-1} from reference [51]:

$$D_C = 4.53 \cdot 10^{-7}(1 + y_C(1 - y_C)\frac{8339.9}{T}exp\{-(\frac{1}{T} - 2.221 \cdot 10^{-4})(17767 - y_C 26436)\} \quad (5.1)$$

where $y_C = x_C/(1 - x_C)$, x_C being the mole fraction of carbon and the temperature T in Kelvin. For a partitioning step of 5 minutes at 450 °C, this yields a diffusion distance of 1.1 µm. Thus carbon enrichment of the untransformed austenite is limited to areas close to the primary martensite lath boundaries. This means that large areas/islands of untransformed austenite do not get uniformly enriched with carbon and will (partially) transform into M_2. Hence, besides suppressing carbide formation, optimizing the size and distribution of the martensite plates could lead to an increase in retained austenite fraction as well. Increasing the A-M boundary area and reducing the size of the untransformed austenite areas are the main points to look at. This is especially relevant for the alloys used in this study because they showed significant microstructural banding, i.e. large separated areas of mostly primary martensite and untransformed austenite.

5.3 Assessment of segregation effects

To investigate the influence of Mn and Cr segregation on the formation and spatial distribution of primary martensite, the primary martensite fractions upon quenching to 156 °C were calculated using Equations 4.1 and 4.2. Calculations were performed for the upper and lower bounds of the Mn and Cr concentration as measured using EPMA and the concentrations of the other elements were considered to be equal to the nominal composition. The results of the calculations are shown in Table 5.1.

Table 5.1: Influence of Mn and Cr segregation on local M_S temperature and volume fraction of primary martensite for a MedCMn specimen with QT equal to 156 °C.

Alloy MedCMn QT = 156 °C	Concentration (wt%)	M_S (°C)	f_{M_1}
Cr/Mn-poor region	11.9Cr-2.7Mn	218	0.65
Cr/Mn-rich region	13.2Cr-3.2Mn	187	0.41
Alloy composition	12.5Cr-3Mn	202	0.54

These calculations demonstrate that Mn and Cr segregation can have a significant effect on the homogeneity of the final microstructure of Q&P processed specimens. The fraction of primary martensite in Cr/Mn-poor and Cr/Mn-rich regions can vary approximately 25 vol% for this particular example (alloy MedCMn with QT equal to 156 °C). Because retained austenite forms along M_1 grains, the retained austenite follows the same spatial distribution as the primary martensite. Thus the elemental segregation into bands also leads to a non-uniform distribution of retained austenite and potentially anisotropy of the mechanical properties of the alloys. Based on Equation 4.1, the segregation of Mn had a similar impact on the local M_S temperature as the segregation of Cr in alloy MedCMn. The microstructural banding in alloy MedC was less pronounced than in alloy MedCMn, which can be attributed to the lower Mn concentration of the alloy.

Banded microstructures may or may not be detrimental to finished steel products but it has been shown that replacing martensite concentrated into bands with randomly dispersed small volumes of martensite can improve subsequent machining and cold forming operations.[23] In a recently published paper by Forouzan et al. [52] it was shown that lower quenching temperatures lead to a decrease in the banding phenomenon in Mn-Cr alloyed Q&P steels. Therefore, the optimal quenching temperature is represented by considering the balance between the banding formation, the retained austenite fraction and the carbon concentration of the retained austenite. Finding this temperature requires extensive research and should be evaluated for each particular chemical composition and application.

Chapter 6

Conclusions and Recommendations

6.1 Conclusions

In this thesis, two novel stainless steels with compositions 0.2C-0.35Si-0.7Mn-12.5Cr (MedC) and 0.2C-0.35Si-3.0Mn-12.5Cr (MedCMn) were investigated. Specimens of both alloys were subjected to a series of Q&P treatments with varying quenching temperatures. The resulting microstructures were studied using X-ray diffraction, optical microscopy, EBSD, EPMA and phase field simulation. The main conclusions of the study are as follows:

- Mn addition lowers the optimal quenching temperature and increases the maximum retained austenite fraction that can be obtained by applying a Q&P treatment to martensitic stainless steels. Retained austenite phase fractions of approximately 0.22 and 0.3 were obtained by quenching to 183 °C and 142 °C for alloy MedC and MedCMn, respectively.
- The carbon concentration of retained austenite increases with decreasing quenching temperature. However, in both alloys the carbon enrichment is much lower than the carbon concentrations expected from the full partitioning assumption. The non-uniform distribution of primary martensite and untransformed austenite as well as carbide precipitation are seen as a means by which austenite enrichment and retention are reduced. The carbon concentration of the retained austenite was lower in the high-Mn steel compared to the low-Mn steel.
- The optimal quenching temperature can be predicted correctly using an empirical equation for M_S and experimental measurement of the kinetics of martensite formation.
- A combination of optical microscopy and EBSD can be used to model carbon partitioning with phase field simulations. Simulations and experiments showed that stabilization of untransformed austenite is not only dependent on primary martensite fraction but also on primary martensite morphology and distribution.
- Segregation of Mn and Cr affects the local M_S temperature and causes microstructural banding of primary martensite which leads to a non-uniform retained austenite distribution in the final microstructure.

6.2 Recommendations

Based on the findings in this study, the following is recommended for future work:

- For more precise determination of the retained austenite fraction in heat-treated samples, other characterization techniques such as saturation magnetization could be investigated. Methods that require careful surface preparation (XRD and EBSD) proved to be unreliable.
- The partitioning conditions were fixed in this study and can be further optimized. Different holding times or partitioning temperatures could lead to more uniform carbon enrichment of the untransformed austenite. At the same time, it is important to study and minimize the extent of carbide precipitation during the partitioning step.
- Because the material used in this study was already homogenized at 1270 °C for 3 hours, longer homogenization treatments will likely not be (cost) effective to reduce Mn and Cr segregation and the associated microstructural banding. Reducing the prior austenite grain size (PAGS) through a grain-refining heat treatment could be investigated as a means for creating microstructures with a more homogeneous distribution of austenite.
- Through mechanical characterization techniques such as tensile testing, the relationship between microstructure and mechanical properties can be investigated. Moreover, the optimal combination of retained austenite fraction and carbon concentration can be identified. It can also be interesting to study the differences in the mechanical stability of the retained austenite between the two alloys. These experiments can help to determine which of the two alloys has the most potential for commercial applications and further development.

Bibliography

[1] D.K. Matlock and J.G. Speer. "Third generation of AHSS: microstructure design concepts". In: *Microstructure and texture in steels*. Springer, 2009, pp. 185–205.

[2] J.G. Speer et al. "Carbon partitioning into austenite after martensite transformation". In: *Acta materialia* 51.9 (2003), pp. 2611–2622.

[3] J.G. Speer, E. De Moor, and A.J. Clarke. "Critical assessment 7: quenching and partitioning". In: *Materials Science and Technology* 31.1 (2015), pp. 3–9.

[4] J. Mola and B.C. De Cooman. "Quenching and partitioning (Q&P) processing of martensitic stainless steels". In: *Metallurgical and Materials Transactions A* 44.2 (2013), pp. 946–967.

[5] T. Tsuchiyama et al. "Microstructure control of a low carbon martensitic stainless steel by quenching and partitioning heat treatment". In: *Materials Science Forum*. Vol. 706. Trans Tech Publ. 2012, pp. 2338–2341.

[6] J. Tobata et al. "Role of silicon in quenching and partitioning treatment of low-carbon martensitic stainless steel". In: *ISIJ international* 52.7 (2012), pp. 1377–1382.

[7] T. Tsuchiyama et al. "Quenching and partitioning treatment of a low-carbon martensitic stainless steel". In: *Materials Science and Engineering: A* 532 (2012), pp. 585–592.

[8] Q. Huang et al. "Influence of martensite fraction on tensile properties of quenched and partitioned (Q&P) martensitic stainless steels". In: *steel research international* 87.8 (2016), pp. 1082–1094.

[9] Z.Z. Zhao et al. "The influence of the austempering temperature on the transformation behavior and properties of ultra-high-strength TRIP-aided bainitic–ferritic sheet steel". In: *Materials Science and Engineering: A* 613 (2014), pp. 8–16.

[10] O. Matsumura, Y. Sakuma, and H. Takechi. "Enhancement of elongation by retained austenite in intercritical annealed 0.4 C-1.5 Si-O. 8Mn Steel". In: *Transactions of the Iron and Steel Institute of Japan* 27.7 (1987), pp. 570–579.

[11] RINA-CSM, Acerinox Europa, IMDEA Materials Institute & Delft University of Technology. *Development of New Martensitic Stainless Steels for Automotive Lightweight Structural Applications (QPINOX)*. `https://www.qpinox.eu/`.

[12] J.G. Speer et al. "The "quenching and partitioning" process: background and recent progress". In: *Materials Research* 8.4 (2005), pp. 417–423.

[13] M. Hillert and J. Ågren. "On the definitions of paraequilibrium and orthoequilibrium". In: *Scripta Materialia* 50.5 (2004), pp. 697–699.

[14] J.G. Speer et al. "Comments on "On the definitions of paraequilibrium and orthoequilibrium" by M. Hillert and J. Ågren, Scripta Materialia, 50, 697–9 (2004)". In: *Scripta Materialia* 52.1 (2005), pp. 83–85.

[15] M. Hillert and J. Ågren. "Reply to comments on "On the definition of paraequilibrium and orthoequilibrium"". In: *Scripta Materialia* 52.1 (2005), pp. 87–88.

[16] E. Seo and B.C. De Cooman. "Quenching and Partitioning (Q&P) Processing of AISI 420 Stainless Steel". In: *Proceedings of the 8th Pacific Rim International Congress on Advanced Materials and Processing*. Springer. 2013, pp. 809–817.

[17] Q. Huang, H. Biermann, and J. Mola. "Influence of martensite fraction on the extent of partitioning in martensitic stainless steels processed by quenching and partitioning (Q&P)". In: *8th European Stainless Steel Conference, Graz*. 2015.

[18] H.K.D.H Bhadeshia and R. Honeycombe. *Steels: microstructure and properties*. Butterworth-Heinemann, 2017.

[19] E. Kozeschnik and H.K.D.H. Bhadeshia. "Influence of silicon on cementite precipitation in steels". In: *Materials Science and Technology* 24.3 (2008), pp. 343–347.

[20] Q. Huang et al. "Influence of Si addition on the carbon partitioning process in martensitic-austenitic stainless steels". In: *IOP Conference Series: Materials Science and Engineering*. Vol. 373. 1. IOP Publishing. 2018, p. 012001.

[21] M.C. Flemings and G.E. Nereo. "MACROSEGREGATION. PT. 1". In: *AIME Met Soc Trans* 239.9 (1967), pp. 1449–1461.

[22] F. HajyAkbary et al. "A quantitative investigation of the effect of Mn segregation on microstructural properties of quenching and partitioning steels". In: *Scripta Materialia* 137 (2017), pp. 27–30.

[23] G. Krauss. "Solidification, segregation, and banding in carbon and alloy steels". In: *Metallurgical and Materials Transactions B* 34.6 (2003), pp. 781–792.

[24] C.G. De Andres et al. "Application of dilatometric analysis to the study of solid–solid phase transformations in steels". In: *Materials Characterization* 48.1 (2002), pp. 101–111.

[25] H.S. Yang and H.K.D.H. Bhadeshia. "Uncertainties in dilatometric determination of martensite start temperature". In: *Materials Science and Technology* 23.5 (2007), pp. 556–560.

[26] D.J. Dyson. "Effect of alloying additions on the lattice parameter of austenite". In: *J. Iron Steel Inst.* 208 (1970), pp. 469–474.

[27] H.K.D.H. Bhadeshia et al. "Stress induced transformation to bainite in Fe–Cr–Mo–C pressure vessel steel". In: *Materials Science and Technology* 7.8 (1991), pp. 686–698.

[28] ASTM E407-07. *Standard Practice for Microetching Metals and Alloys*. Standard. ASTM International, 2015.

[29] R. Witt and M. Nowell. "Specimen preparation of difficult materials for EBSD characterization". In: *Microscopy and Microanalysis* 17.S2 (2011), pp. 414–415.

[30] J.T. Armstrong. "Quantitative elemental analysis of individual microparticles with electron beam instruments". In: *Electron probe quantitation*. Springer, 1991, pp. 261–315.

[31] ASTM E975-13. *Standard Practice for X-Ray Determination of Retained Austenite in Steel with Near Random Crystallographic Orientation*. Standard. ASTM International, 2013.

[32] C.F. Jatczak. "Retained Austenite and its Measurement by X-ray Diffraction". In: *SAE Transactions* (1980), pp. 1657–1676.

[33] C. Garcia-Mateo et al. "On measurement of carbon content in retained austenite in a nanostructured bainitic steel". In: *Journal of materials science* 47.2 (2012), pp. 1004–1010.

[34] B.D. Cullity. *Elements of X-ray Diffraction*. Addison-Wesley Publishing, 1956.

[35] S.S. Babu et al. "In-situ observations of lattice parameter fluctuations in austenite and transformation to bainite". In: *Metallurgical and Materials Transactions A* 36.12 (2005), pp. 3281–3289.

[36] D. Peckner and I.M. Bernstein. *Handbook of stainless steels*. McGraw-Hill New York, 1977.

[37] S. Dieck et al. "Reversed austenite for enhancing ductility of martensitic stainless steel". In: *IOP conference series: materials science and engineering*. Vol. 181. 1. IOP Publishing. 2017, p. 012034.

[38] S.Y. Lu et al. "Effect of quenching and partitioning on the microstructure evolution and electrochemical properties of a martensitic stainless steel". In: *Corrosion Science* 103 (2016), pp. 95–104.

[39] K.W. Andrews. "The calculation of transformation temperatures and austenite-ferrite equilibrium in steels". In: *Journal of the Iron and Steel Institute* 184 (1956), p. 414.

[40] C.Y. Kung and J.J. Rayment. "An examination of the validity of existing empirical formulae for the calculation of M_S temperature". In: *Metal. Trans. A* 13.2 (1982), pp. 328–331.

[41] Q. Huang et al. "Dilatometry analysis of dissolution of Cr-rich carbides in martensitic stainless steels". In: *Metallurgical and Materials Transactions A* 48.12 (2017), pp. 5771–5777.

[42] D. Aichbhaumik et al. *Heat Treatment Procedure Qualification: Final Technical Report, US Department of Energy Contract No.* Tech. rep. DE-FC07-99ID13841, 2004.

[43] T. Sourmail and V. Smanio. "Determination of M s temperature: methods, meaning and influence of 'slow start'phenomenon". In: *Materials Science and Technology* 29.7 (2013), pp. 883–888.

[44] D.P. Koistinen and R.E. Marburger. "A general equation prescribing the extent of the austenite-martensite transformation in pure iron-carbon alloys and plain carbon steels". In: *Acta metallurgica* 7 (1959), pp. 59–60.

[45] S.M.C. Van Bohemen and J. Sietsma. "Effect of composition on kinetics of athermal martensite formation in plain carbon steels". In: *Materials science and technology* 25.8 (2009), pp. 1009–1012.

[46] R. Pradhan and G.S. Ansell. "Kinetics of the martensite transformation in athermal Fe-C-Ni-Cr alloys". In: *Metallurgical Transactions A* 9.6 (1978), pp. 793–801.

[47] M.J. Dickson. "The significance of texture parameters in phase analysis by X-ray diffraction". In: *Journal of applied Crystallography* 2.4 (1969), pp. 176–180.

[48] Z. Nishiyama. *Martensitic transformation*. Elsevier, 2012.

[49] M.G. Mecozzi et al. "Phase field modelling of microstructural evolution during the quenching and partitioning treatment in low-alloy steels". In: *Computational Materials Science* 112 (2016), pp. 245–256.

[50] D.A. Porter, K.E. Easterling, and M.Y. Sherif. *Phase Transformations in Metals and Alloys*. CRC press, 2009.

[51] J. Agren. "A revised expression for the diffusivity of carbon in binary Fe-C austenite". In: *Scripta metallurgica* 20.11 (1986), pp. 1507–1510.

[52] Farnoosh Forouzan et al. "Optimization of quenching temperature to minimize the micro segregation induced banding phenomena in quenching and partitioning (Q&P) steels". In: *steel research international* 90.1 (2019), p. 1800281.